Zwaan et al. *Swiss Journal of Geosciences* (2022) 115:26
https://doi.org/10.1186/s00015-022-00427-8

SGG SGS sc | nat
Swiss Journal of Geosciences

ORIGINAL PAPER Open Access

Influence of rheologically weak layers on fault architecture: insights from analogue models in the context of the Northern Alpine Foreland Basin

Frank Zwaan[1,2*], Guido Schreurs[1], Herfried Madritsch[3] and Marco Herwegh[1]

Abstract

We present a series of analogue models inspired by the geology of the Zürcher Weinland region in the Northern Alpine Foreland Basin of Switzerland to explore the influence of rheological weak, i.e. (partially) ductile layers on the 3D evolution of tectonic deformation. Our model series test the impact of varying weak layer thickness and rheology, as well as different kinematics of an underlying "basal fault". Model analysis focuses on deformation in the weak layer overburden and, uniquely, within the weak layer itself. We find that for low to moderate basal fault displacements, the above-mentioned parameters strongly influence the degree of coupling between the basal fault and the weak layer overburden. Coupling between the basal fault and overburden decreases by reducing the strength of the weak layer, or by increasing the weak layer's thickness. As a result, basal fault displacement is less readily transferred through the weak layer, leading to a different structural style in the overburden. By contrast, increasing the amount, or rate, of basal fault slip enhances coupling and leads to a more similar structural style between basal fault and overburden. Moreover, dip-slip displacement on the basal fault is more readily transferred to the overburden than strike-slip displacement of the same magnitude. Our model results compare fairly well to natural examples in the Northern Alpine Foreland Basin, explaining various structural features. These comparisons suggest that rheological weak layers such as the Jurassic Opalinus Clay have exerted a stronger control on fault zone architecture than is commonly inferred, potentially resulting in vertical fault segmentation and variations in structural style. Furthermore, the novel addition of internal marker intervals to the weak layer in our models reveals how complex viscous flow within these layers can accommodate basal fault slip. Our model results demonstrate the complex links between fault kinematics, mechanics and 3D geometries, and can be used for interpreting structures in the Alpine Foreland, as well as in other settings with similar weak layers and basal faults driving deformation in the system.

Keywords: Analogue modelling, Tectonics, Rheology, Weak layers, Northern Alpine Foreland Basin

1 Introduction

The role of mechanical stratigraphy during tectonic deformation and its effect on fault architecture is widely recognized (e.g. Childs et al., 1996; Ferrill et al., 2017; Laubach et al., 2009, and references therein). Rheologically weak rock layers can result in decoupling of deformation between units below and above these weak layers. Typical examples of such weak layers are shale, gypsum or salt intervals, and their decoupling effect due to a

Editorial handling: Stefan Schmid

*Correspondence: frank.zwaan@geo.unibe.ch

[1] Institute of Geological Sciences, University of Bern, Baltzerstrasse 1+3, 3012 Bern, Switzerland
Full list of author information is available at the end of the article

(partially) ductile rheology may cause deformation styles in the overburden to differ greatly from those in the units below the weak layer (e.g. Ferrill & Morris, 2008; Ferrill et al., 2007, 2017; Stewart, 2007; Stewart & Clark, 1999).

Recently, the relevance of mechanical stratigraphy for fault development has also been recognized in the context of the Northern Alpine Foreland Basin (Roche et al., 2020; Shipilin et al., 2020; Fig. 1). In the "Zürcher Weinland" region of Northern Switzerland (Figs. 1, 2), 3D seismic data indicates that the Jurassic Opalinus Clay represents a significant rheologically weak layer across which displacement along underlying faults (referred to as "basal faults" in this paper) was (partially) buffered and/or decoupled from deformation in its overburden (Fig. 2a, c; Nagra, 2001; Roche et al., 2020). Only recently, drilling results in that same area revealed that the Opalinus Clay indeed shows only minor signs of faulting or fracturing, even within deformation zones identified on seismic reflection data (Nagra, 2022). Elsewhere in the Swiss Alpine Foreland, sub-surface fault interpretations can, with few exceptions (e.g. Heuberger et al., 2016; Nagra, 2019a, 2019b, 2019c), only rely on 2D seismic data (e.g. Allenbach et al., 2017; Gruber, 2017; Madritsch et al., 2018; Mock & Herwegh, 2017; Sommaruga et al., 2012). This lack of 3D data prevents a thorough (3D) assessment of possible effects of mechanical stratigraphy and basal fault kinematics on deformation in both the overburden and the weak layer itself. With only limited additional constraints from outcrops and earthquake data (Diehl et al., 2021; Egli et al., 2017; Vouillamoz et al., 2017), other approaches need to be considered to improve our understanding of deformation in the NW Alpine Foreland, and similar tectonic settings elsewhere.

One such approach is the use of analogue tectonic modelling, which has since long been proven to be an excellent means to systematically explore the evolution of (3D) tectonic deformation over time in settings involving basal faults and a weak layer (e.g. Richard, 1989, 1991; Withjack & Callaway, 2000). Analogue modelling studies focusing on pure dip-slip normal faulting have shown that various factors have an impact on the degree of decoupling caused by the presence of a viscous layer. In general, coupling, and thus efficient transfer of deformation into the overburden is affected by, e.g., weak layer thickness and viscosity, overburden thickness and cohesion, basal fault displacement and -slip rate (Withjack & Callaway, 2000). Other researchers have studied factors such as the alteration of competent layers and clay smear in similar dip-slip systems (e.g. Kettermann et al., 2017; Schmatz et al., 2010; Vrolijk et al., 2016). Also the first-order influence of oblique dip-slip and strike-slip have been explored through analogue models (Richard, 1989, 1991; Richard et al., 1995). Even so, the detailed 3D structural evolution of such systems has received only limited attention and thus remains poorly constrained, especially when it comes to deformation within the weak layer.

In this study, we use a series of analogue models inspired by the Zürcher Weinland, an area within the Swiss Alpine foreland with a comparatively well constrained geological and tectonic setting (Figs. 1b, c, 2). Our aim is to explore the influence of weak layers and basal fault kinematics on the 3D evolution of deformation in the overburden and, uniquely, within the weak layer. We subsequently compare our model results with natural examples, and whereas the model set-up is tailored to simulate the geological setting in the Swiss Alpine Foreland, we find that our novel results can also serve for interpreting the structural evolution of similar settings elsewhere around the globe.

2 Geological setting and modelling context

The Zürcher Weinland of northern Switzerland is situated in the NW part of the Northern Alpine Foreland Basin (Fig. 1b; Sommaruga et al., 2012). This region is characterized by a stratigraphy marked by pronounced rheological contrasts that is comprehensively registered in the sequence drilled at Benken (Nagra, 2001; Roche et al., 2020; Fig. 2b) and has undergone a polyphase tectonic history (Egli et al., 2017; Madritsch, 2015; Marchant et al., 2005 and references therein).

The crystalline basement of northern Switzerland is dissected by major Late Paleozoic grabens (Permo-Carboniferous troughs; e.g. Allenbach et al., 2017; Diebold et al., 1991; Madritsch et al., 2018; Marchant et al., 2005; Sommaruga et al., 2012) that formed during a phase of post-orogenic extension following the Variscan orogeny (Echtler & Chauvet, 1992; Eisbacher et al., 1989). The Benken borehole does not reveal any Permo-Carboniferous sediments and is therefore interpreted to be located on a structural horst in between these troughs (Fig. 2b; Marchant et al., 2005; Roche et al., 2020). The subsequent Mesozoic sequence was deposited in the context of the opening of the Alpine Tethys and large-scale transgression, starting with an approximately 350 m thick

(See figure on next page.)

Fig. 1 General tectonic setting. **a** Tectonic overview map of the broader Northern Alpine Foreland Basin. *Ap.* Apennines. Modified after Sommaruga et al. (2012). **b** Tectonic map of the Swiss Alpine Foreland. *BWFZ* Burgdorf-Wynigen Fault Zone, *SGFZ* Sankt Gallen Fault Zone, *ZWL* Zürcher Weinland. Modified after Sommaruga et al. (2012). **c** Map of Northern Switzerland (around Schaffhausen, including the Zürcher Weinland, of which a detailed map is provided in Fig. 2a). *FBBFZ* Freiburg-Bonndorf-Bodensee Fault Zone, *HLCG* Hegau-Lake Constance Graben, *NHFZ* Neuhausen Fault Zone, *RDF* Randen Fault, *RMF* Rafz-Marthalen Flexure, *ZWL* Zürcher Weinland. Modified after Roche et al. (2020)

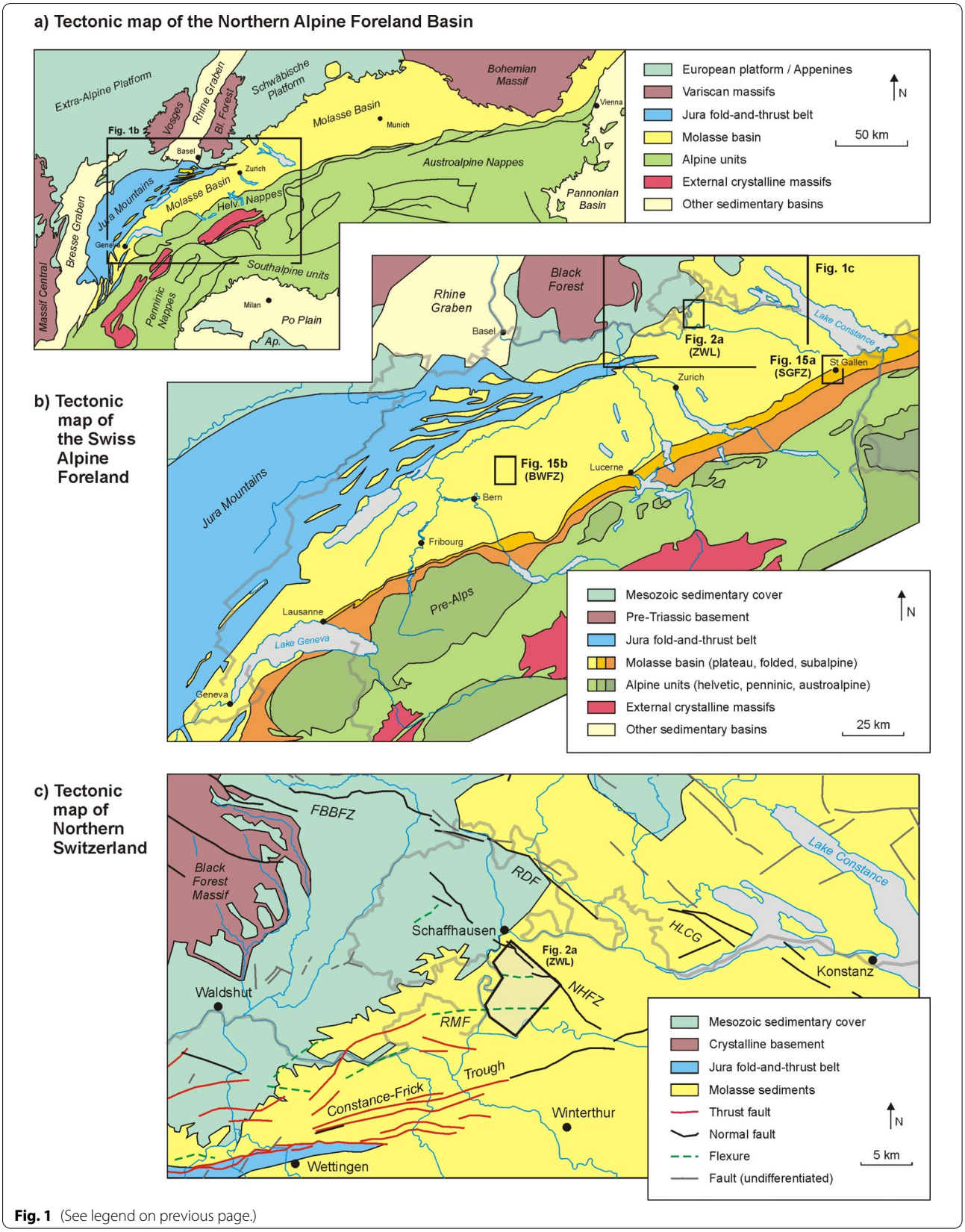

Fig. 1 (See legend on previous page.)

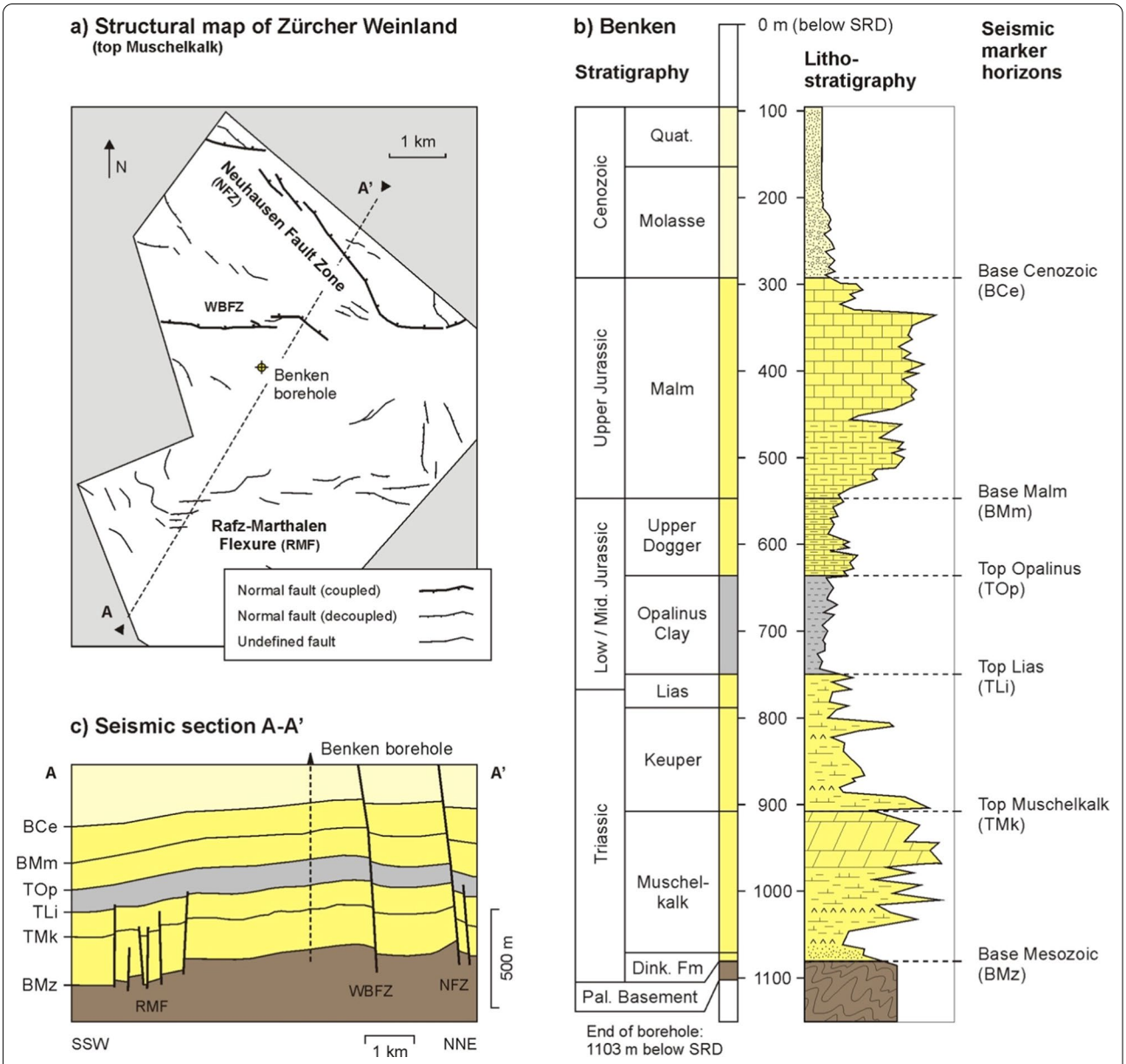

Fig. 2 Geology of the Zürcher Weinland (modified after Roche et al., 2020). **a** Simplified structural map of structures showing fault traces at Top Muschelkalk level according to 3D seismic interpretation. WBFZ: Wildenbuch Fault Zone. Decoupled faults do not cross the Opalinus Clay, coupled faults do (see [**c**]). Map location shown in Fig. 1b. **b** Local stratigraphy as revealed in the Benken borehole (location shown in [**a**]), showing the relative rheological weakness of the Opalinus Clay compared to the units above and below, based on Young's modulus data from laboratory tests (see Roche et al., 2020 for details). Note that Permo-Carboniferous units were not encountered in this particular borehole. SRD: Seismic Reference Datum (here 500 m above sea level). **c** Interpreted seismic section A-A', showing the location of the Opalinus Clay (in grey) and its effect on coupling between the units above and below. For the full names of the seismic horizons, see (**b**). NHF: Neuhausen Fault Zone, RMF: Rafz-Marthalen Flexure, WBFZ: Wildenbuch Fault Zone

sequence of Triassic (incl. Liassic) evaporites, carbonates and marls, followed by the comparatively homogeneous and rheologically weak ca. 120 m thick Opalinus Clay Formation deposited in the Middle Jurassic (Amann et al., 2017; Hostettler et al., 2017; Nagra, 2001; Roche et al., 2020; Fig. 2b). The lithological characteristics of the Dogger sediments overlying the Opalinus Clay vary compositionally and rheologically. In the Zürcher Weinland an approximately 80 m thick mechanically weak marly succession is developed. Further to the west this succession is laterally replaced by mechanically stiffer limestones (Bläsi et al., 2013, and references therein).

The upper Jurassic Malm group is dominated by limestones intercalated with marls and is generally more competent. Across the wider Northern Alpine Foreland Basin, the thickness of this succession varies greatly due to a regional unconformity at its upper limit, marking a late Eocene phase of crustal-scale uplift that was driven by the development of the early Alpine forebulge and resulted in several hundred meters of erosion (Kempf & Pfiffner, 2004; Mazurek et al., 2006; Roche et al., 2020; Schori, 2021; Sinclair & Allen, 1992; von Hagke et al., 2012). Consequently, no Cretaceous units are preserved in the Zürcher Weinland and the resulting thickness of the Upper Jurassic limestones and marls amounts to some 250 m (Fig. 2b).

The present-day structural characteristics of the Zürcher Weinland are largely the result of its Cenozoic tectonic history. During Eocene and Oligocene times the area was presumably influenced by the evolution of the roughly N-S trending European Cenozoic Rift System (ECRIS; (e.g. the Rhine and Bresse Grabens; Fig. 1a; Dèzes et al., 2004; Hinsken et al., 2007; Schori, 2021; Ziegler, 1992). During this tectonic phase, the Mesozoic sequence across the entire Swiss foreland basin was affected by N-S striking faults (Gruber, 2017). Only thereafter, the actual North Alpine foreland Molasse sedimentation set in, which consisted of 4 mega-sequences of clastics, deposited in a flexural foreland basin (Pfiffner, 1986; Sinclair & Allen, 1992; Willett & Schlunegger, 2010). Basin subsidence is inferred to have resulted in reactivation of basement faults leading to the formation of monoclines and normal faults striking roughly parallel to the basin axis (Diebold & Noack, 1997; Gruber, 2017; Malz et al., 2016). The Zürcher Weinland area at the northern rim of the Swiss Molasse Basin was additionally impacted by NE-SW directed extension related to the Middle Miocene formation of the Hegau-Lake Constance graben leading to the formation of normal faults oblique to the basin axis (Egli et al., 2017, Figs. 1c, 2a) and associated Hegau volcanism (Ibele, 2015, and references therein). The Zürcher Weinland area was not affected by large-scale thin-skinned Alpine folding and thrusting (Fig. 1a and c; Burkhard, 1990; Gruber, 2017; Sommaruga et al., 2012; Vouillamoz et al., 2017).

The most recent evolution of the Swiss Molasse Basin including the Zürcher Weinland (Pliocene to present) saw a phase of large-scale erosion (Cederbom et al., 2011; Von Hagke et al., 2012) and transition to thick-skinned tectonics involving reactivation of deep-seated faults, most commonly as strike-slip faults (Heuberger et al., 2016; Mock & Herwegh, 2017). Seismological data indicates that some of these faults are active until the present day (Diehl et al., 2015, 2021; Mock & Herwegh, 2017; Vouillamoz et al., 2017).

Within the context of the complex tectonic history of the Northern Alpine Foreland Basin, our analogue model set-up is tailored to the Zürcher Weinland (Figs. 1b, c, 2). Accordingly, the models are designed to simulate the Middle Jurassic Opalinus Clay as an important weak layer separating the basin's sedimentary sequence in a lower and upper part (Fig. 2b, c). Introducing a steeply dipping "basal fault" underneath the weak layer aims to simulate the Swiss Molasse Basin's tectonic setting during the Middle Miocene to recent times when basement-rooted faults (e.g. the Rafz-Marthalen Flexure [RMF] and Neuhausen Fault Zone [NHFZ], Figs. 1c, 2a, c) became reactivated in various ways depending on their orientation with respect to the regional stress field. Thereby we explore if and under what conditions the weak Opalinus Clay influenced the deformation in the overlying the sedimentary sequence.

3 Methods

3.1 General model set-up

We apply a model set-up involving a deformable base to simulate a basal fault that induces deformation in an overlying weak layer, which itself is overlain by a more competent overburden, thus reproducing the tectonic setting in the Zürcher Weinland (Figs. 2, 3). The total thickness of these model materials is set to 6.5 cm, representing the 650 m of stratigraphy measured from the base of the Opalinus Clay Formation to the surface (Fig. 2c). The deformable base consists of a mobile and a fixed base plate that are both 2 cm thick, with the contact between these two base plates representing a steep, 75° dipping fault plane (or velocity discontinuity: VD), similar to the faults present in the Northern Alpine Foreland Basin (Figs. 1c, 2a, c, 3a, b, e). Furthermore, each base plate is attached to a longitudinal sidewall. The space between this longitudinal sidewall is 30 cm, and the length of the set-up is ca. 80 cm (Fig. 3b). The mobile base plate, together with its attached sidewall, can move outward (y-axis), downward (z-axis) and right-laterally (x-axis) by means of precise computer-controlled motors (Fig. 3a–c). By combining these three motions, we can simulate either pure normal dip-slip, 45° (dextral) oblique normal slip, or pure dextral strike-slip fault kinematics, as defined on the basal fault plane (Fig. 3b, e).

3.2 Model materials

Granular materials have been commonly applied for simulating brittle materials in the Earth's crust (e.g. Klinkmüller et al., 2016; Panien et al., 2006). We model the brittle overburden overlying the Opalinus Clay Formation in the Alpine foreland using quartz sand (Quarzsand A) from Carlo Bernasconi AG (www.carloag.ch) (Table 1). This quartz sand has a grain size of 60–250 µm, internal

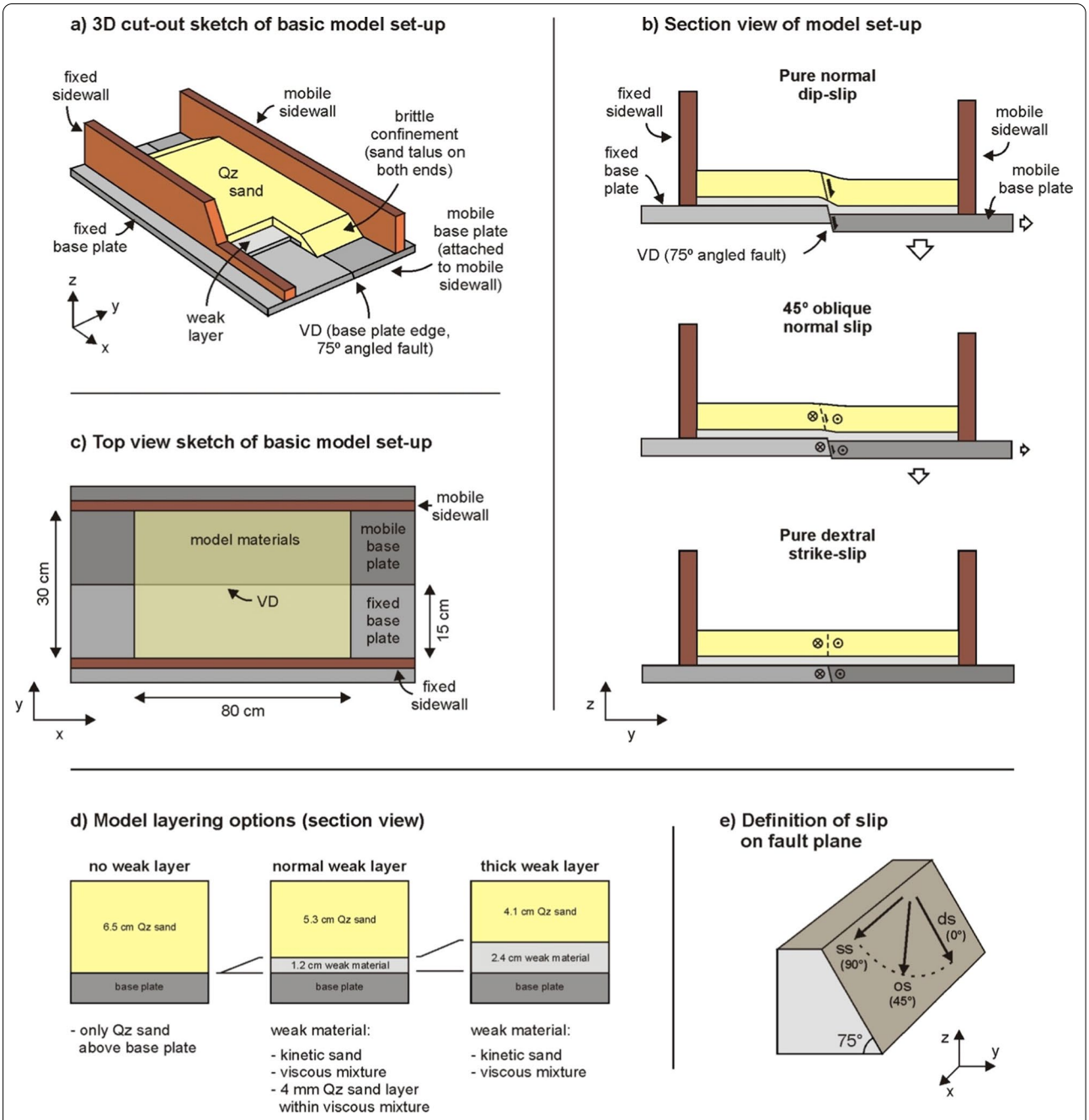

Fig. 3 Model set-up. **a** 3D sketch of basic model set-up. **b** Section view sketches depicting the different kinematics we apply in our models (pure normal dip-slip, 45° oblique normal dip-slip and pure dextral strike-slip along the basal fault). **c** Top view sketch of model set-up. **d** Different types of weak layers applied in our models. Note that the total model thickness is always kept at 6.5 cm, translating to 650 m in nature (Fig. 2b). **e** Definition of slip direction on the basal fault as applied in our models. ds: pure (normal) dip-slip (0°), os: (45°) (dextral) oblique normal slip, ss: (pure dextral) strike-slip (90°). Note that the oblique normal slip is a combination of pure normal dip slip and pure strike-slip, the combined vector of which yields the required oblique slip direction. Slip rates applied in our models are defined in the direction of slip. *Qz* quartz, *VD* velocity discontinuity

friction angles in the order of 31.4°–36.1° (Table 1), and a cohesion value of 9 Pa (Zwaan et al., 2018). Furthermore, it has a density of 1560 kg/m^3 when sieved from a height of c. 30 cm (Schmid et al., 2020). For creating internal markers within the quartz sand to visualize deformation in cross-sections (see Sect. 3.5), we insert thin (< 1 mm) intervals of corundum sand (F120 Normalkorund from Carlo Bernasconi AG). The rheology of the corundum

Table 1 Properties of granular materials

Material	Quartz sand[a]	Corundum sand[b]	Feldspar sand[c]
Grain size (ø)	60–250 µm	88–125 µm	100–250 µm
Grain density ($\rho_{specific}$)	2650 kg/m^3	3960 kg/m^3	ca. 2650 kg/m^3
Density (sieved) (ρ_{sieved})	1560 kg/m^3	1890 kg/m^3	1300 kg/m^3
Internal peak friction angle (φ_p)	36.1°	37°	33°
Dynamic-stable friction angle (φ_p)	31.4°	32.2°	29.7°
Reactivation friction angle (φ_p)	33.4°	33.8°	32°
Cohesion (C)	9 ± 98 Pa	39 ± 10 Pa	5–10 Pa

[a] Properties after Zwaan et al. (2018)

[b] Properties after Panien et al. (2006), used for internal layering (see Appendix A for details)

[c] Properties after Zwaan et al. (2022c), used for internal layering (see Appendix A for details)

Table 2 Properties of kinetic sand

Material	Kinetic sand[a]
Grain size (ø)	150 µm (mean)
Weight mixing ratio (granular / PDMS)	98 / 2
Grain density ($\rho_{specific}$)	ca. 2650 kg/m^3
Density (bulk) (ρ_{bulk})	ca. 1600 kg/m^3
Rheology	"Brittle-viscous"
Internal peak friction angle (φ_p)	31.0°
Dynamic-stable friction angle (φ_p)	29.2°
Reactivation friction angle (φ_p)	30.5°
Cohesion (C)	251 ± 325 Pa

[a] Properties after Katz et al. (2014) and Mayolle et al. (2021), and from new ring-shear tests done at GFZ Potsdam. Kinetic sand is a brittle-viscous material, but considered to be dominated by brittle component of its rheology since standard rheometer tests for viscous material testing (e.g. Rudolf et al. 2016) were not possible due to the material's limited capacity to flow. Bulk density measured in Bern.

Table 3 Properties of viscous material

Material	Viscous mixture[a]
Weight mixing ratio (granular / silicone)	1 / 1
Density (bulk) (ρ_{bulk})	1600 kg/m^3
Viscosity (η)	1.5×10^5 Pa s
Rheology	Near-Newtonian (n = 1.06–1.10)

[a] Properties after Zwaan et al. (2018c)

sand is very similar to that of the quartz sand (Table 1), and the inclusion of the thin marker intervals is not considered to significantly affect model evolution.

In order to simulate the weak Opalinus Clay Formation in our models we use one of two types of "weak" materials, i.e. materials that exhibit (partial) viscous behaviour when deformed, reproducing the ductile character of the clay (Tables 2, 3). The first of these is kinetic sand, a material produced by Spin Master (www.spinmaster.com), which is a mixture of 98% quartz sand (mean grain size: 150 µm) and 2% of silicone oil (polydimethylsiloxane, or PDMS) coating the sand grains (Katz, 2014; Mayolle et al., 2021). The PDMS in the kinetic sand causes it to have a somewhat visco-brittle behaviour (Mayolle et al., 2021), a internal friction angle of c. 29.5°–31°, and a relatively high cohesion value of ca. 250 Pa as determined through ring-shear tests at GFZ Potsdam (following the procedures of e.g. Klinkmüller et al., 2016 and Ritter et al., 2016), whereas the density of the material is ca. 1600 kg/m^3. Kinetic sand has been successfully applied by Mayolle et al. (2021) for simulating the brittle-viscous transition in the deeper parts of the crust, and in this paper we present the first application of this material for simulating a weak layer within the shallower parts of the upper crust. Similar to the quartz sand, we introduce thin (< 1 mm) marker intervals to the kinetic sand. These intervals consist of white FS900F feldspar sand from Amberger Kaolinwerke (https://www.quarzwerke.com) (Table 1, Zwaan et al., 2022c), and are not considered to meaningfully influence the model results.

The second material we use to simulate a weak layer in our models is a mixture of silicone oil (SGM-36 type PDMS, formerly produced by Dow Corning, now part of Dow Chemical (www.dow.com), and the aforementioned F120 corundum sand from Carlo Bernasconi AG. This mixture, made with a ca. 1:1 weight-mixing ratio, has a density of ca. 1600 kg/m^3 (Zwaan et al., 2018). Whereas the kinetic sand with its transitionary rheology is still relatively competent compared to the quartz sand representing the brittle overburden, this mixture of PDMS and corundum sand is truly viscous and represents a very weak end-member of Opalinus Clay behaviour. The material has a near-Newtonian rheology (n = 1.06–1.10), and a viscosity of ca. 1.5×10^5 Pa s at typical model strain rates of $< 10^{-4}$/s (Zwaan et al., 2018). This material has been applied in various modelling studies, either as a lower crustal analogue (e.g. Schmid et al., 2022; Zwaan

et al., 2016, 2019) or as an upper crustal weak layer in contractional models (e.g. Schori et al., 2021). Similar to the kinetic sand, we use thin (< 1 mm) marker intervals of feldspar sand to trace deformation in cross-sections, the presence of which does not significantly alter the model results.

A final, combined option we use for simulating an overall weak layer is the inclusion of a thin quartz sand layer within a layer of the viscous PDMS-corundum sand mixture. This quartz sand layer then represents a unit of more competent sediments (e.g. a sandstone or carbonate interval) within the weak layer. Information on how these model layers are prepared is provided in the Appendix.

3.3 Model parameters

In this study we present the results of 13 analogue models (out of a total of 18 completed models runs, see supplementary material in Zwaan et al., 2022b). These 13 models are sub-divided in four main series (Table 4). The first two model series (Series A and B) are aimed at exploring the influence of weak layers in pure dip-slip systems, and the second two model series (Series C and D) explore the influence of other basal fault kinematics and basal fault slip rate, respectively.

Series A contains our reference models, with a standard (weak) layer thickness of 1.2 cm simulating the 120 m thick Opalinus Clay Formation (Fig. 2c). This layer is overlain by a 5.3 cm [530 m] strong and brittle overburden of quartz sand, Figs. 2c, 3d), and basal fault slip rates are 10.4 mm/h during a 1-h model run (translating to 4.1 mm/yr in nature, see Sect. 3.4). In these models we test the influence of different types of weak layer rheology. This series comprises models with a weak layer made of either kinetic sand (Model A2), of the viscous mixture (Model A4), or of the viscous mixture with a 4 m thick internal sand layer (Model A3). In addition, we include a model without a weak layer (Model A1); instead, this model has a total brittle layer thickness of 6.5 cm (650 m).

In our Series B models we explore the effect of increasing the weak layer thickness (doubling it to 2.4 cm, or 240 m in nature, with 4.1 cm or 410 m of brittle overburden to keep the scaling identical to the other models, allowing for direct comparison). The weak layers in Models B1 and B2 consist of kinetic sand and the viscous mixture, respectively. Basal fault slip rates and direction are the same as in Series A, i.e. 10.4 mm/h pure normal dip-slip, for a model run duration of 1 h. Note that no model with a sand-only layering is included in this series since the strain-rate independent behaviour of granular materials means that the results of such a model would simply be the same as those of Model A1.

The models in Series C serve to test the effect of 45° dextral oblique normal slip on the basal fault plane (Models C1 and C2) and pure dextral strike-slip fault kinematics (Models C3 and C4) (for definitions of oblique slip and strike-slip motion, see Sect. 3.1 and Fig. 3e). Here, Models C1 and C3 are sand-only (6.5 cm thick), thus lacking a weak layer, whereas the 1.2 cm thick weak layer in Models C2 and C4 consists of the viscous mixture. No models with kinetic sand layers are included in this

Table 4 Overview of model parameters

Series	Model	Weak layer	Basal fault kinematics[a]
Series A (reference models)	A1	Sand-only (without weak layer)	Pure normal dip-slip
	A2	Kinetic sand	Pure normal dip-slip
	A3	Quartz sand layer in viscous mixture[b]	Pure normal dip-slip
	A4	Viscous layer	Pure normal dip-slip
Series B (models with a thick weak layer)[c]	B1	Kinetic sand[c]	Pure normal dip-slip
	B2	Viscous layer[c]	Pure normal dip-slip
Series C (oblique slip & strike-slip models)	C1	Sand-only (without weak layer)	Dextral oblique normal slip
	C2	Viscous mixture	Dextral oblique normal slip
	C3	Sand-only (without weak layer)	Pure dextral strike-slip[d]
	C4	Viscous mixture	Pure dextral strike-slip[d]
Series D (fast fault slip models)[e]	D1	Kinetic sand	Pure normal dip-slip
	D2	Viscous mixture	Pure normal dip-slip
	D3	Viscous mixture	Pure dextral strike-slip[d]

[a] For definition of basal fault kinematics, see Sect. 3.1 and Fig. 3e

[b] Layering includes a 4 mm thick quartz sand layer within the 1.2 cm thick weak layer

[c] Weak layer is 2.4 cm thick and brittle quartz sand overburden is 4.1 cm thick to maintain a total model thickness of 6.5 cm

[d] Total basal fault slip in the strike-slip models is increased by a factor two, to 20.8 mm

[e] Basal fault sliplip rate increased by a factor 10 to 104 mm/h (compared to standard 10.4 mm/h). Accordingly, the total model duration is reduced by a factor 10 as well

series, and basal fault slip rates in Series C are the standard 10.4 mm/h (where the duration of strike-slip Models C3 and C4 is doubled to obtain a total basal fault slip of 20.8 mm). Note that the 10.4 mm/h 45° oblique normal slip in Models C1 and C2 is a combination of 7.4 mm/h normal dip slip and 7.4 mm mm/h pure dextral strike-slip (see Fig. 3e).

Our Series D models aim to elucidate the influence of strain rate on model evolution by increasing basal fault slip rates by a factor of ten (104 mm/h). The models in this series have a standard weak layer thickness of 1.2 cm. We apply pure dip-slip deformation for Models D1 (kinetic sand layer) and D2 (viscous mixture layer), and dextral strike-slip for Model D3 (viscous mixture layer). The tenfold increase of basal fault slip velocity means that the model run duration is reduced by a factor of 10 to 6 min for pure dip-slip Models D1 and D2, and 12 min for pure dextral strike-slip model D3. Therefore, direct comparisons can be made with the relevant models from Series A and C. Note that similar to Series B, no sand-only models are included in Series D due to the strain-rate independent behaviour of granular materials.

3.4 Scaling

The main concern for scaling purposes in brittle materials, which exhibit strain-rate independent behaviour, is the angle of internal friction. This angle lies between 33.4° and 36.1° for our quartz sand, which is very similar to friction angles measured for rocks in the uppermost kilometres of the crust (ca. 40°, Byerlee, 1978, a value also measured for rocks from the Benken borehole, Giger & Marschall, 2014; Roche et al., 2020, Table 5). Although kinetic sand has a viscous component to its behaviour due to the presence of PDMS silicone oil, we can still assume a somewhat brittle behaviour. The internal friction angle of the kinetic sand lies between 31° and 29.5°, which is lower than that of the pure quartz sand and very similar to the friction angle of the Opalinus Clay as measured in the Benken borehole (ca. 30°, Giger & Marschall, 2014; Roche et al., 2020). Here it may be noted that the material has a higher cohesion than the quartz sand (Tables 1, 2, 5), and could as such be considered stronger than the quartz sand under typical model conditions. However, the partial viscous behaviour of the kinetic sand causes it to deform in a similar fashion to shales (such as the Opalinus Clay) in nature (Mayolle et al., 2021). We can thus consider the kinetic sand a "weak" material due to its viscous behaviour, which is not fully captured by ring-shear tests that are designed for purely brittle materials.

The scaling of purely viscous materials such as our viscous PDMS/corundum sand mixture becomes more complex than the scaling of brittle materials due to their strain rate-dependent rheology. We can use the stress ratio between model and nature (σ^*, convention: $\sigma^* = \sigma_{model}/\sigma_{nature}$): $\sigma^* = \rho^*\ h^*\ g^*$, where ρ^*, h^* and g^* are the density, length and gravity ratios, respectively (Hubbert, 1937; Ramberg, 1981), in combination with the viscosity ratio (η^*) to obtain the strain rate ratio $\dot{\varepsilon}^*$ (Weijermars & Schmeling, 1986): $\dot{\varepsilon}^* = \sigma^*/\eta^*$. With the strain rate ratio we can subsequently compute the velocity and time ratios (v^* and t^*): $\dot{\varepsilon}^* = v^*/h^* = 1/t^*$. If we consider the Opalinus Clay as a viscous rather than a brittle material in nature, and adopt a somewhat high viscosity of 5×10^{17} Pa s for the Opalinus Clay (Yarushina et al., 2021), the viscosity of 1.5×10^5 Pa s of our viscous model material makes that an hour of deformation in the laboratory translates to ca. 25 kyr in nature. Therefore our

Table 5 Scaling parameters

	Model material	Nature[a]
Material	Quartz sand	Overburden
Density ($\rho_{specific}$)	1560 kg/m^3	2700 kg/m^3
Internal peak friction angle	36.1°	ca. 40°
Cohesion	9 Pa	20 MPa (2 MPa[b])
Material	Kinetic sand	Opalinus Clay (strong end-member)
Density ($\rho_{specific}$)	1600 kg/m^3	2400–2500 kg/m^3
Internal peak friction angle	31°	ca. 30°
Cohesion	251 Pa	3 MPa
Material	Viscous mixture	Opalinus Clay (weak end-member)
Density ($\rho_{specific}$)	1600 kg/m^3	2400–2500 kg/m^3
Viscosity (η)	1.5×10^5 Pa s	5×10^{17} Pa s

[a] Natural values adopted from Giger and Marschall (2014), Roche et al. (2020), and Yarushina et al. (2021)

[b] Experimentally measured cohesion values of natural rocks may be one or even two degrees of magnitude lower in natural situations due to initial heterogeneities, or weakening caused by preceding tectonic deformation (Von Hagke et al., 2019)

standard basal fault slip rate of 10.4 mm/h is scaled down to a reasonable 4.1 mm/yr.

We furthermore consider the dynamic similarity between our models and the natural example in the North Alpine foreland. In the case of the brittle materials we use the ratio Rs between the gravitational stress and the cohesive strength or cohesion C (Mulugeta, 1988; Ramberg, 1981): R_s = gravitational stress/cohesive strength = (ρ g h)/C. Assuming the natural cohesion of 20 MPa for the sedimentary layers overlying the Opalinus Clay to be reduced by an order of magnitude due to weakening factors (Table 5), combined with the quartz sand cohesion of 9 Pa, we obtain a R_s value of 17 and 1.3 for model and nature, respectively. Cohesion in our modelled overburden thus seems somewhat low but is quite acceptable; our quartz sand cohesion value may in reality be higher, given the error margins (Table 1), and cohesion values of bulk rocks in natural situations may be even more reduced (Von Hagke et al., 2019). In the case of viscous materials, we use the Ramberg number R_m (Weijermars & Schmeling, 1986): R_m = gravitational stress/viscous strength = (ρ g h^2)/(η v). Here we find a R_m value of ca. 3.6 for both the viscous mixture and the Opalinus Clay. Since both the R_s and R_m values of our model materials were practically the same as their equivalents in nature, we consider our models to be reasonably scaled.

3.5 Model monitoring and analysis

We apply a number of methods for monitoring and analysing our analogue models. The first method involves time-lapse photography of the model surface by means of a rig containing three computer-controlled high-resolution Nikon D810 cameras (e.g. Schmid et al., 2022; Zwaan et al., 2021a, 2022a). Map view time-lapse imagery in combination with a surface grid made of corundum sand (< 1 mm thick) allows a first-order visual assessment of model evolution (Fig. 4a). Further model analysis involves photogrammetry analysis of images from the (obliquely oriented) cameras (using Agisoft Photoscan, www.agisoft.com) to obtain digital elevation models for topography analysis in open source QGIS software (www.qgis.org), (Fig. 4b).

Quantification of surface deformation is done by digital image correlation (DIC) analysis of time lapse imagery using DaVis 10.1 from LaVision (www.lavision.de), which allows for analysis of horizontal displacements and strain (Fig. 4c). Of particular interest are the maximum normal strain and minimum normal strain, representing the changes to the long and short axes of the strain ellipse, serving as proxies for normal and reverse faulting, respectively (e.g. Zwaan et al., 2021a, 2022a). For strike-slip models, we use shear strain instead. The interval for DIC analyses is 2.6 mm of basal fault slip.

In addition, we produce cross-sections of our models by wetting and cutting the models to reveal internal model deformation, assisted by the presence of marker intervals (Fig. 4d). In contrast to standard model sectioning, which is done at the end of a model run (since the sectioning procedure destroys the model), we took advantage of the models' physical length to produce progressive sections at 2.6 mm basal fault slip intervals, creating pseudo-time-lapse series of model sections (Fig. 4a, d). This progressive sectioning method has to our knowledge only been sparsely used (e.g. Burliga et al., 2012), but allows unique insights into internal model evolution, especially through the novel use of marker intervals within the simulated weak layer. In order to capture lateral variations in model structure, various sections are made for each interval, (see also the supplementary material, Zwaan et al., 2022b), of which representative sections are selected for further structural analysis (Fig. 4a, d). This analysis involves fault interpretation by tracing vertical offsets of 1 mm or more of the marker intervals within both the simulated weak layer and its brittle overburden, whereas faults with smaller offsets in the overburden may be visible as linear features with a slight colour deviation due to local dehydration of the sand (Fig. 4d).

Using this sectioning method means that parts of the model domain are progressively removed over time (Fig. 4a–c). Therefore, we focus our model analysis on the domains that remain at the end of the model run for surface analysis (Fig. 4c). Note that due to the relative lack of visible (surface) deformation in models with strike-slip deformation, sections are only taken at the end of the model run in these specific models.

4 Model results

4.1 Series A: weak layer rheology

Model results from Series A reveal how the rheology of the weak layer affects deformation in normal dip-slip systems (Figs. 5 and 6). Model A1 is our reference model without a weak layer, Model A2 contains a weak layer consisting of kinetic sand, Model A3 involves a viscous weak layer with a 4 mm thick sand layer incorporated within, and Model A4 has a fully viscous weak layer. All four models involve pure dip slip deformation at a rate of 10.4 mm/h along the basal fault.

The results of reference Model A1 show how initial deformation (after 15 min, or 2.6 mm fault slip along the basal fault) creates an offset and a monocline at the base of the sand layers that dies out towards the model surface (Fig. 5$a_{I–IV}$). However, DIC results indicate increased horizontal displacement compared to the general background displacement, which is bounded by a zone of extension and a zone of contraction (Fig. 5a). The results from the next model step (after 30 min, or 5.6 mm of

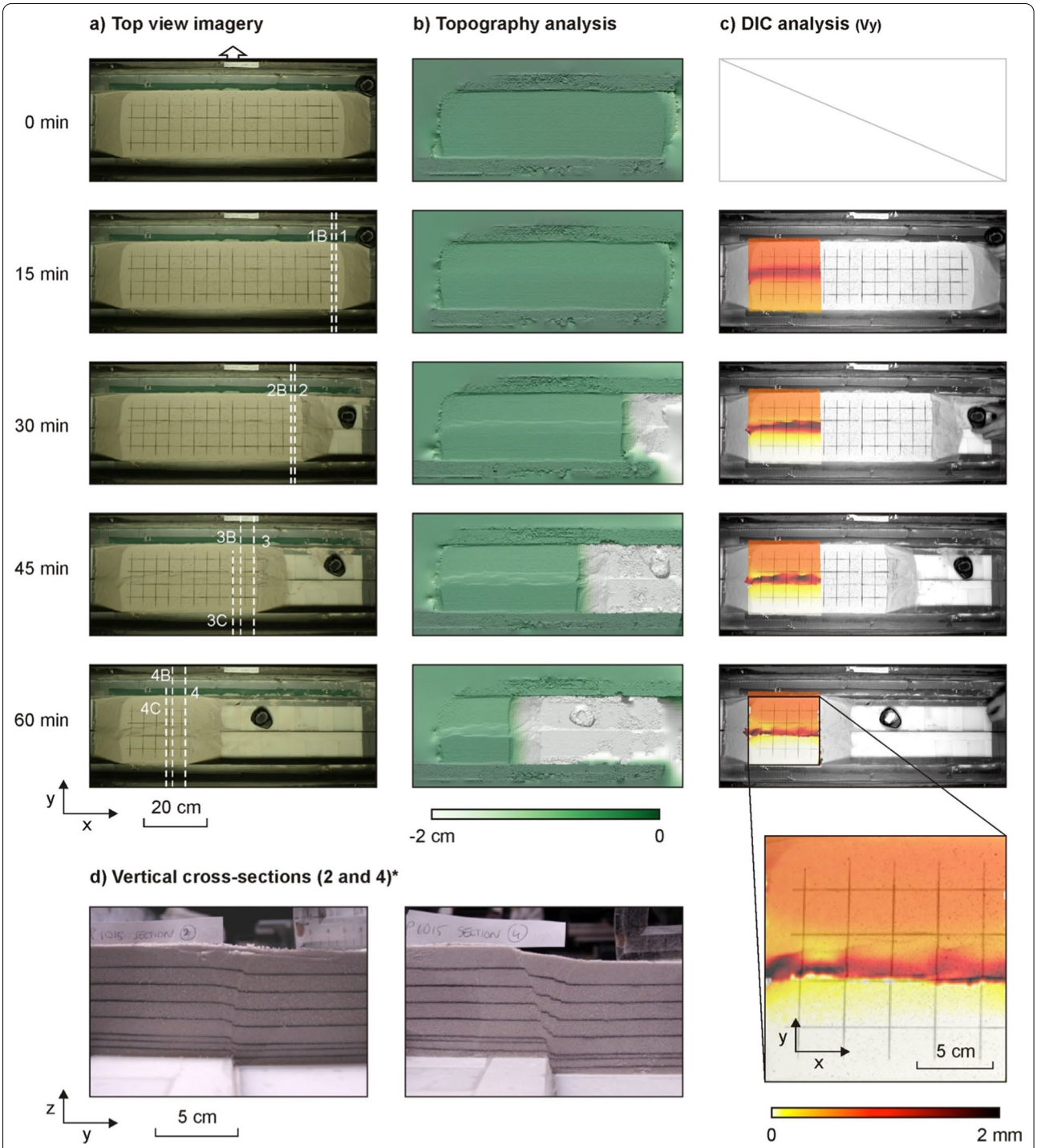

Fig. 4 Model analysis methods (examples taken from Model A1). **a** Time-lapse map view imagery, showing the stepwise reduction of the model length due to repeated sectioning. **b** Topography analysis over time. **c** Example of digital image correlation (DIC) analysis (incremental displacement along the y-axis [Vy]) and selection of area of interest for detailed analysis). **d** Examples of vertical cross-sections (locations shown in [**a**]). Offsets in marker horizon as well as linear colour differences are used to identify (incipient) faults. (*) Note that no vertical distortion is applied when showing vertical cross-sections, so that their horizontal and vertical scaling is identical

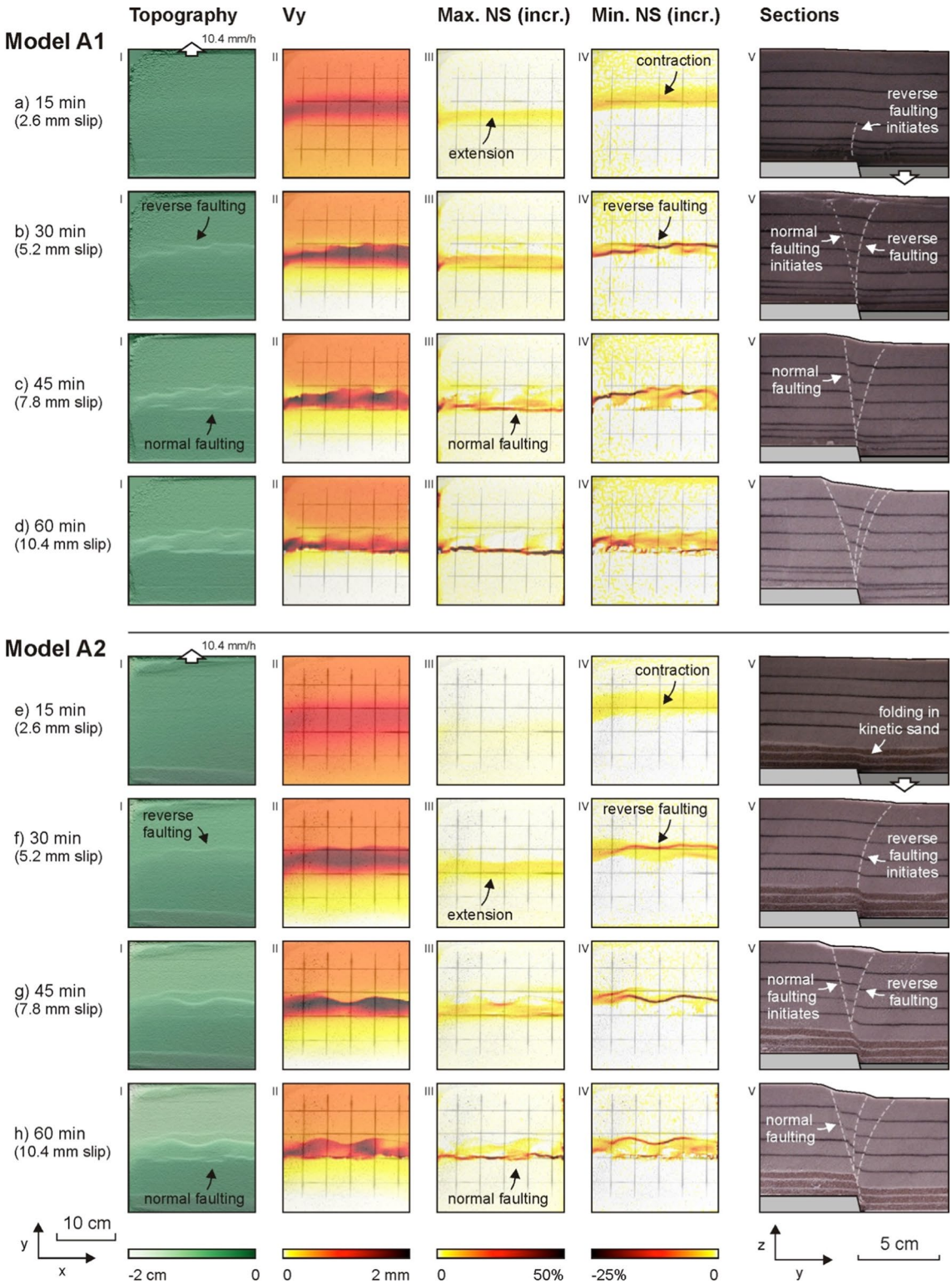

Fig. 5 Overview of model results from Series A, part 1: Pure normal dip-slip along the basal fault, in model without weak layer in Model A1, and with a kinetic sand weak layer in Model A2. Max. / Min. NS (incr.): Incremental maximum / minimum normal strain, indicating extension and contraction in the model, respectively. Vy: incremental displacement in the y-direction. Note that section locations are not indicated due to the progressive sectioning method (see Sect. 3.5 and Fig. 4)

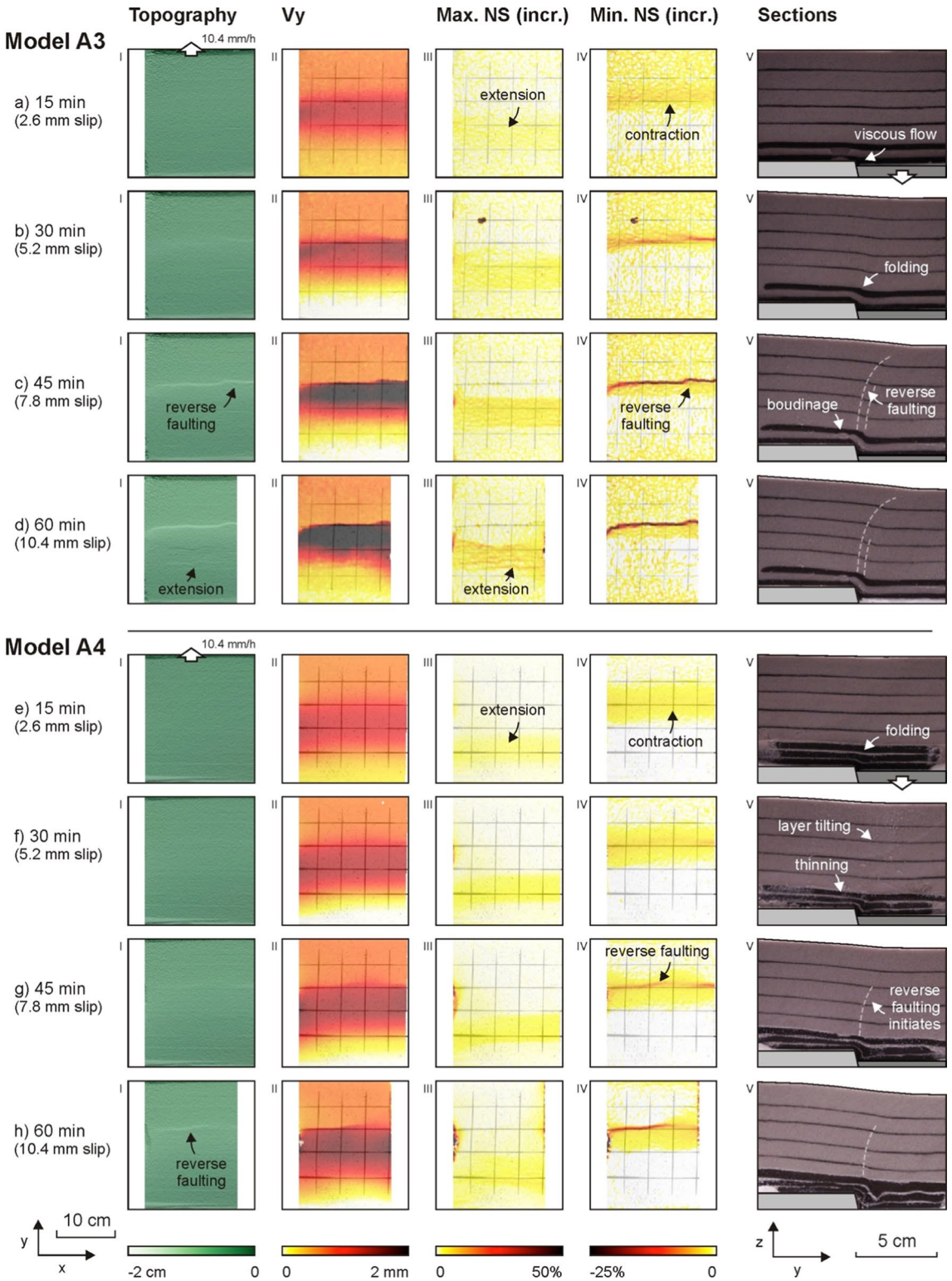

Fig. 6 Overview of model results from Series A, part 2: Pure normal dip-slip along the basal fault, with a sand interval in the viscous detachment layer in Model A3, and with a full viscous detachment in Model A4. Max. / Min. NS (incr.): Incremental maximum / minimum normal strain indicating extension or contraction in the model, respectively. Vy: incremental displacement in the y-direction. Note that section locations are not indicated due to the progressive sectioning method (see Sect. 3.5 and Fig. 4)

fault slip), reveal how the monocline develops into a curved reverse fault that reaches the surface (Fig. 5b). Next to this reverse fault, a normal fault also forms above the basement fault, and becomes better defined on the Maximum Normal Strain maps (Fig. 5b_{III}). As the model continues evolving, the normal fault becomes more pronounced (Fig. 5c, d). Note how there is some curving of the reverse faults along-strike, whereas the normal faults are fairly straight along-strike (Fig. 5a–d).

Model A2 with kinetic sand follows a very similar evolution as Model A1 (Fig. 5), including the development of a zone of increased horizontal displacement, and of a reverse fault prior to the formation of a normal fault. However, the appearance of these faults is somewhat delayed when compared to Model A1 with the kinetic sand in Model A2 buffering initial slip along the underlying basal fault (Fig. 5a, e). As Model A2 evolves, the kinetic sand is faulted in a similar fashion to the sand in Model A1 (Fig. 5a–d, c, d). Yet also here some buffering by the kinetic sand is visible in section view, as the fault zone in the kinetic sand layer in Model A2 is clearly less localized compared to the fault in Model A1 (Fig. 5).

In Model A3, with a thin sand layer intercalated within the weak viscous mixture layer, the structures are rather different from those seen in Models A1 and A2 (Figs. 5, 6a–d). Initial deformation in Model A3 (after 15 min, or 2.6 mm of basal fault slip) seems to be mostly buffered by the weak layer and no clear deformation is visible in top or section view imagery (Fig. 6a). Even so, some distributed contraction and a hint of extension appears on the DIC maps, which border a relatively broad zone of enhanced horizontal displacement (Fig. 6$a_{II–IV}$). As deformation continues (after 20 min, or 5.6 mm of slip), this pattern remains in place, and DIC data show a reverse fault having formed, even though this fault is not yet apparent in section view (Fig. 6b). Note that this slight discrepancy may be due to the section being taken from a different part of the model than where the surface view analyses is done (see Sect. 3.5). With on-going deformation, the reverse fault becomes clearly present in section view as well (Fig. 6c_V). However, in contrast to Models A1 and A2, the reverse fault does not traverse the weak layer (Figs. 5, 6a–d). Instead, the viscous layers seem to buffer the deformation by folding, and the internal sand layer passively follows this folding. In order to accommodate the associated stretching, it develops boudinage features (Fig. 6c_V, d_V). Importantly, no clear normal fault is formed in what is essentially a large monocline bounded by a reverse fault in Model A3, even though some distributed extension is observed on DIC results too (Fig. 6d_{III}).

Finally, Model A4 pushes further the general structural style already observed in Model A3 (Fig. 6). Also in this model (A4), the viscous material strongly buffers deformation induced by the basal fault, so that only limited localized deformation occurs in the brittle overburden (Fig. 6e-h). Instead, we observe a very broad zone of horizontal displacement, and a general tilting of the overburden towards the hanging wall block of the basal fault (well visible in cross-section, e.g. Figure 6h_V). Yet, some reverse faulting is observed, but it is much less expressed and occurs late when compared to the other models (Figs. 5, 6). Similar to Model A3, very little extension is observed, and no clear normal faulting develops in Model A4 (Fig. 6). Instead, it seems that the buffering of deformation in the viscous layer is achieved by significant thinning of the viscous material above the footwall of the basal fault, and by contraction and folding above the hanging wall block, directly adjacent to the basal fault (see cross-section, Fig. 6h_V). All the time, the contact with the brittle overburden remains rather undeformed, even if it is tilted.

4.2 Model B series models: thick weak layer

The model results from Series B, with a double weak layer thickness (2.4 cm) and pure normal dip-slip, are presented in Fig. 7. In the kinetic sand weak layer case (Model B1), the structural evolution is rather similar to that of Model A2 with the standard weak layer thickness (Figs. 5e–h, 7a–d). In both cases, we observe early reverse faulting after 2.6 mm of basal fault slip (Figs. 5e, 7a), followed by the development of a normal fault after 7.8 mm of slip (Figs. 5g, 7c). The kinetic sand in Model B1 exhibits the same "fault smear" or buffering behaviour as in Model A2 (Figs. 5e–h, 7a–d) (compare to sand-only reference Model A1, Fig. 5a–d). A further important similarity between Models A2 and B1 is that faults seem to nucleate at the interface between the kinetic sand and the quartz sand overburden, as is well illustrated in section view (Figs. 5e–h, 7a–d). However, there is an important difference between both models in that the fault structures in the overburden of Model B1 are smaller in scale with respect to those in Model A2 (Figs. 5e–h, 7a–d).

Where a thicker kinetic sand weak layer does not alter the structural style of Model B1 substantially with respect to its reference counterpart Model A2 (Figs. 5e–h, 7a–d), the doubling of the fully viscous layer in Model B2 causes significant deviations from the structures observed in its reference model counterpart (Model A4) (Figs. 6e–h, 7e–h). The initial stages (after 2.6 mm basal fault slip) in both models are rather similar, involving the development of diffuse contractional and extensional zones (Figs. 6e, 7e). Both models also develop a tilting of the overburden towards the hanging wall of the basal fault, which is accommodated by viscous flow. However, this viscous flow is much more pronounced in Model B2, leading to enhanced thinning of the viscous layer above the footwall

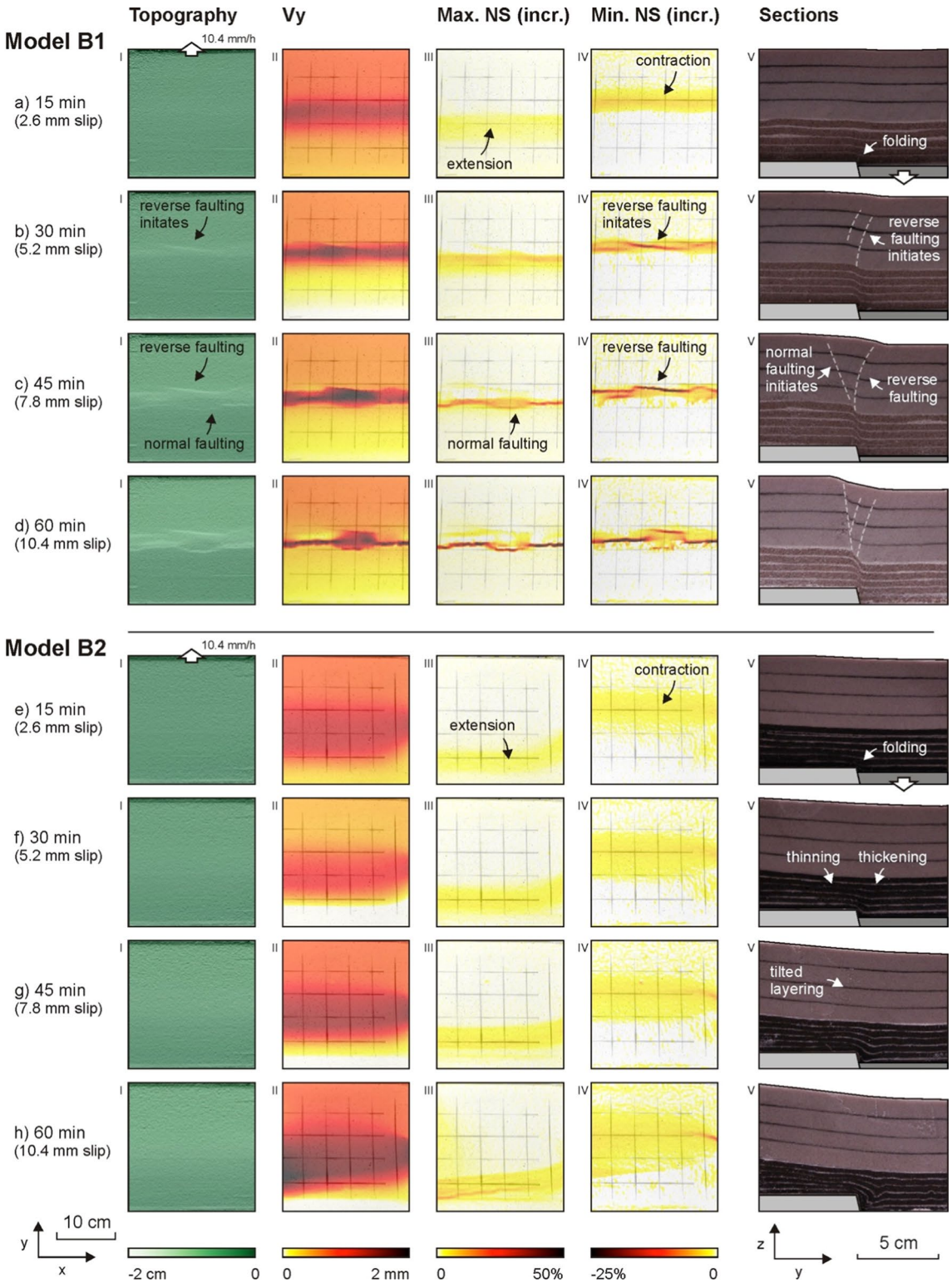

Fig. 7 Overview of model results from Series B: Pure normal dip-slip along the basal fault, with a kinematic sand layer in Model B1, and with a full viscous detachment in Model B2. The weak layers have twice the thickness as those in Series A. Max. / Min. NS (incr.): Incremental maximum / minimum normal strain, indicating extension or contraction in the model, respectively. Vy: incremental displacement in the y-direction. Note that section locations are not indicated due to the progressive sectioning method (see Sect. 3.5 and Fig. 4)

of the underlying fault, and strong thickening and folding within the viscous layer adjacent to the fault (see section views in Figs. 6e–h, 7e–h). Moreover, the interface between the viscous detachment and the brittle sand overburden, although tilted, remains smooth, and no faulting is observed in the quartz sand overburden of Model B2 (Fig. 7e–h), whereas minor reverse faulting can be observed in the overburden of Model A4, Fig. 6e–h).

4.3 Series C: oblique and strike-slip kinematics

Figures 8 and 9 provide overviews of the results from Series C, in which we test the influence of 45° (dextral) oblique normal slip and pure dextral strike-slip kinematics along the basal fault. In the case of the 45° oblique slip Models C1 and C2 (with kinetic sand and viscous weak layer, respectively), we find that the structural evolution is rather similar to that observed in their pure normal dip-slip counterparts (Models A2 and A4, respectively, Figs. 5e–h, 6e–h, 8). Model C1 also develops reverse faults followed by normal faults, and at the same moment as in Model A2, even though these structures are somewhat less evolved in Model C1 than in Model A2 (Figs. 5e–h, 8a–d). Similarly, Model C2 shows the same type of thinning of the viscous detachment above the basal fault footwall, accompanied by the same folding and thickening adjacent to the basal fault as seen in Model A4 (Figs. 6e–h, 8e–h). Also in Model C2, these structures are however somewhat less developed than in its pure normal dip-slip counterpart Model A4 (Figs. 6e–h, 8e–h). Model C2 also develops an oblique fault, which may be a boundary effect (Fig. 8h). Furthermore, there are no clear signs of any strike-slip-related structures in the section views of either Model C1 or C2, even though the strike-slip deformation component is as large as the dip-slip component in these models (Fig. 3e), and strike-slip displacement is clearly visible in surface view imagery (i.e. the deformed surface grid, Fig. 8).

In pure dextral oblique-slip Models C3 and C4, the strike-slip features are poorly developed during the first hour of deformation (Fig. 9a, b, e, f). The only clear hints of strike-slip displacement at this stage in these models come from the deformed surface grid, and from the DIC shear strain analysis (Fig. 9a, b, e, f). However, strike-slip features clearly appear during the second hour of the prolonged model run (2 h, or 20.8 mm basal fault slip) applied for these experiments. In the case of sand-only Model C3, a series of en echelon (Riedel) faults appear, bounding an uplifted central domain (Fig. 9c, d). This uplift is accommodated by the development of a pop-up structure that is visible in section (Fig. 9i, j). These sections also reveal sub-vertical faults with minimal vertical offset (Fig. 9i, j). Together with the surface view data, the sections show that the en echelon faults are in fact (oblique) reverse faults on one side of the model, which become steep strike-slip faults when crossing the model axis, only to become (oblique) reverse faults on the other side of the model again (Fig. 9c, d). Note however, that the oblique slip along the reverse segments of the Riedel faults on opposite sides of the model axis, when present, is also opposite (dextral becomes sinistral or vice versa). However, in Model C4 (with a viscous detachment) these Riedel and pop-up structures are not clearly developed, even in the second hour of the model run (Fig. 9e–h, k, l). Furthermore, any (steep strike-slip) faulting that occurs is propagating from the short ends inward, suggesting such faulting in Model C4 is mostly a boundary effect (Fig. 9e–h, l). What is however clearly visible in section is the thickening of the brittle sand overburden in the centre of the model, leading not only to upward bulging as shown on model topography data, but also to downward bulging of the sand layer into the viscous detachment (Fig. 9e–h, k).

4.4 Series D: influence of increased basal fault slip rate

In the final model Series D we examine the influence of a tenfold higher basal fault slip rate (104 mm/h instead of 10.4 mm/h) on the evolution of models with a weak layer (Figs. 10, 11). In the case of Model D1 that involves a kinetic sand layer and pure normal dip-slip, the development is very similar to that of the equivalent model with a standard, lower, slip rate (Model A2) (Figs. 5e–h, 10a–d). In both models, initial reverse faulting is followed by the development of a normal fault, whereas the kinetic sand layer somewhat buffers basal fault slip by limited folding (compare to the clean faulting in sand-only Model A1, Fig. 5a–d).

By contrast, Model D2 (with a viscous weak layer) shows that increased basal fault slip can lead to significant differences in model evolution (Fig. 10e–h). Instead of allowing the viscous layer to flow, and somewhat buffer basal fault slip by thinning and folding as in Model A4 (Fig. 6e–h), the viscous layer is dragged downward in Model D2 (Fig. 10e–h). This downward drag seems rather similar to the deformation of the kinetic sand in Models A2 and D1 (Figs. 5e–h, 10a–d), and results in the relatively early development of reverse faulting (when compared to Model A4, Figs. 6e–h, 10f). Nevertheless, even though there is some extension apparent in DIC imagery, we do not observe the development of clear normal faulting in Model D2 (Fig. 10e–h).

Whereas increased basal fault slip rate does clearly alter the structural evolution of Model D2, Model D3 does not appear to be much affected by faster slip (Fig. 11). This latter model, which has the same viscous layer as Model D2, but undergoes pure dextral strike-slip deformation, produces the same general structures as its equivalent

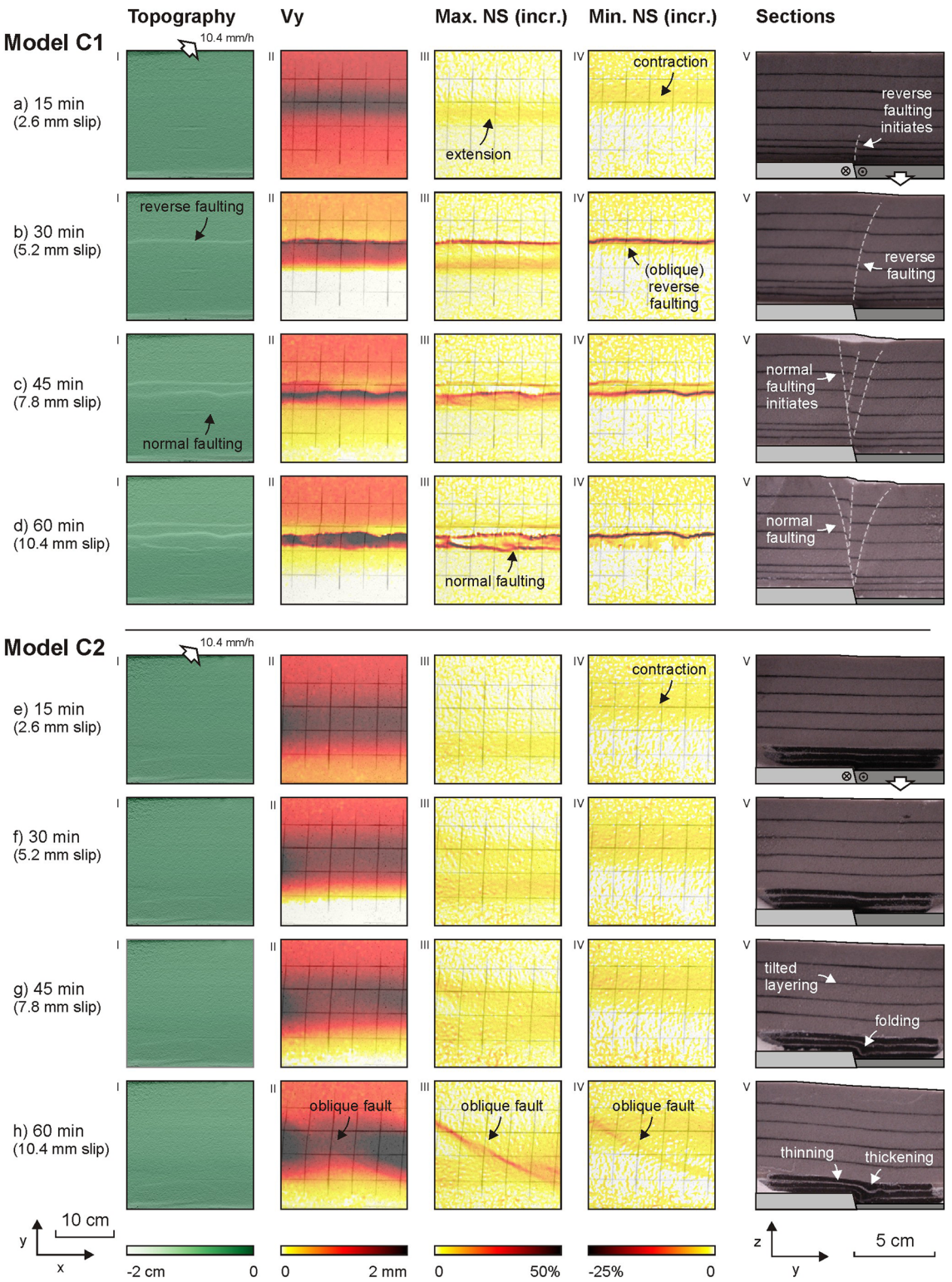

Fig. 8 Overview of model results from Series C, part 1: 45° (dextral) oblique normal slip along the basal fault, without a detachment in Model C1, and with a full viscous detachment in Model C2. Max. / Min. NS (incr.): Incremental maximum / minimum normal strain, indicating extension or contraction in the model, respectively. Vy: incremental displacement in the y-direction. Note that section locations are not indicated due to the progressive sectioning method (see Sect. 3.5 and Fig. 4)

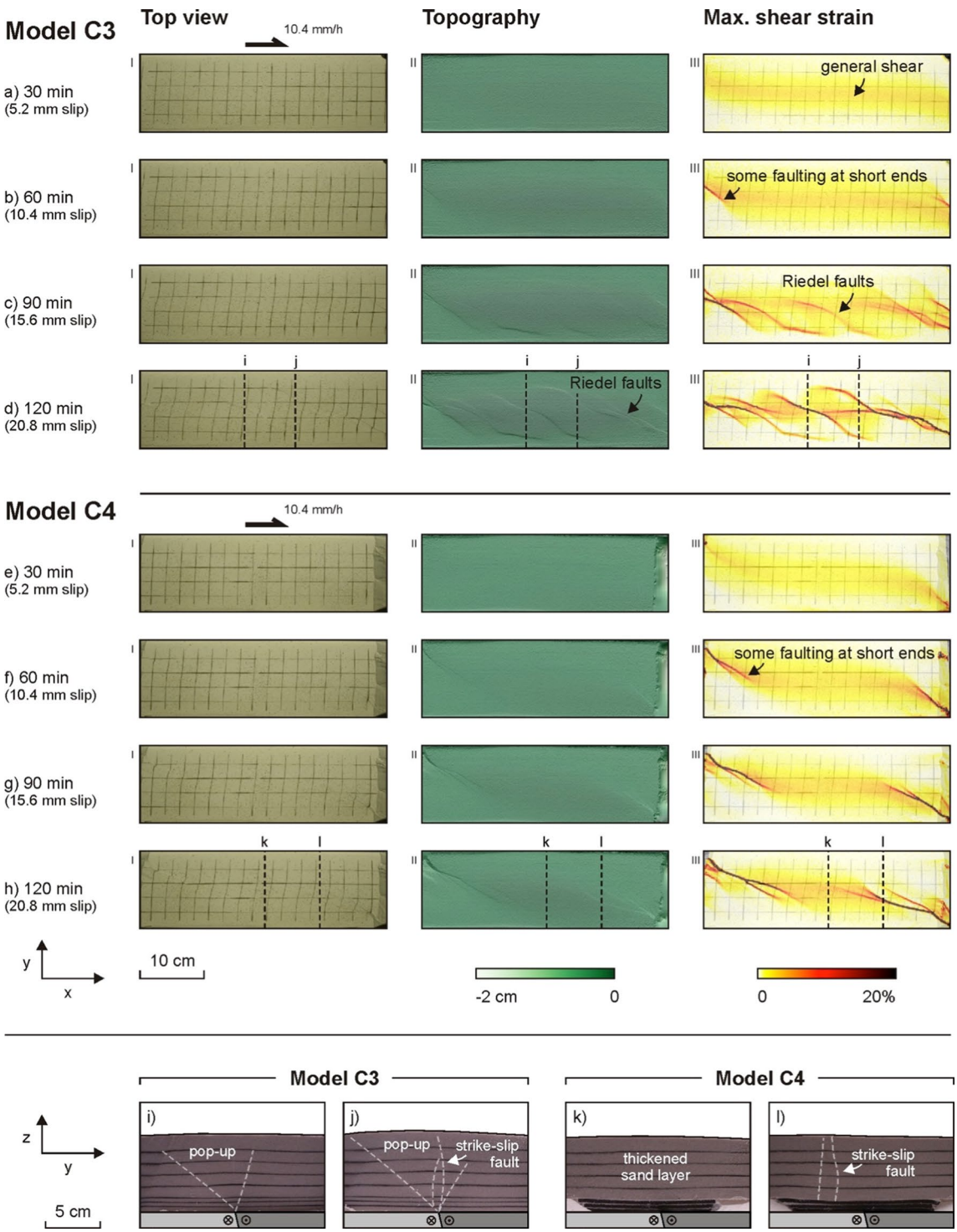

Fig. 9 Overview of model results from Series C, part 2: Pure dextral strike-slip along the basal fault, in model without a viscous weak layer (Model C3) and with a viscous weak layer (Model C4). Total slip is twice as much as in the pure normal dip-slip models and the 45° oblique normal slip models (i.e. 20.8 mm, after a 120 min model run)

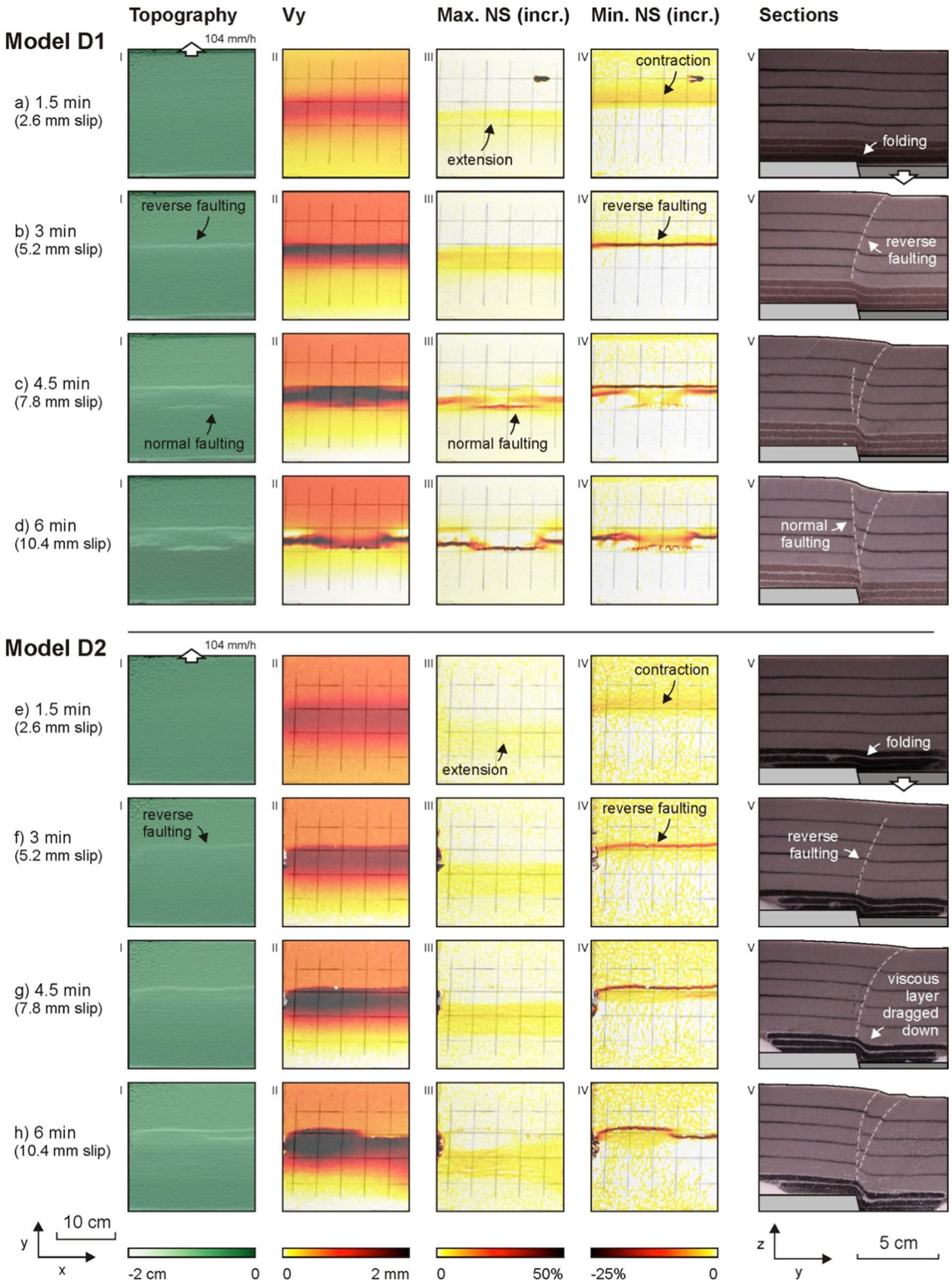

Fig. 10 Overview of model results from Series D, part 1: Pure normal dip-slip along the basal fault, with a kinetic sand layer in Model D1, and with a weak viscous layer in Model D2. Max./Min. NS (incr.): Incremental maximum/minimum normal strain, indicating extension or contraction in the model, respectively. Vy: incremental displacement in the y-direction. Note that section locations are not indicated due to the progressive sectioning method (see Sect. 3.5 and Fig. 4)

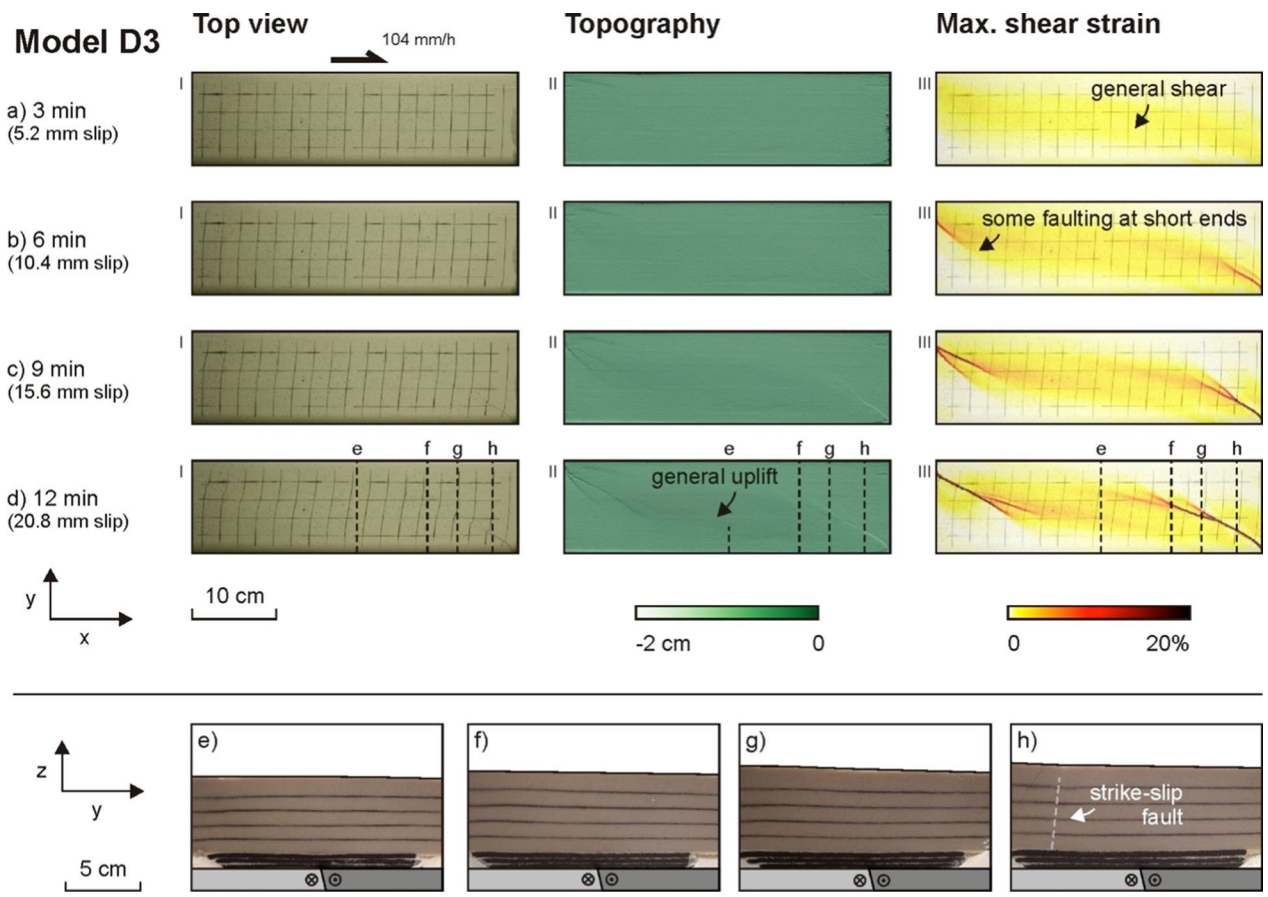

Fig. 11 Overview of model results from Series D, part 2 (Model D3): Pure dextral fast strike-slip along the basal fault with a full viscous layer. Total fault slip is twice as much as in the pure normal dip-slip models and the 45° oblique normal slip models (i.e. 20.8 mm, after a 120 min model run)

with a normal slip rate (Model C4, Figs. 9e–h, 11). In both Model C4 and D2 we observe a lack of distinct faulting until the one-hour-mark, and subsequent faults are propagating from the model short ends inward (Fig. 9e–h, 11). Both models develop uplift along their central axis, even though the downward bulging of the sand layer and the associated thinning of the viscous layer below it, as seen in Model C4, is not as apparent in Model D2 (Figs. 9l, 11e–h).

5 Discussion

5.1 Synopsis of model results

Within the parameter space covered by our models, we find that both model layering and basal fault kinematics have important impacts on fault model evolution (summarized in Figs. 12 and 13). Of these two parameter groups, the impact of model layering is best shown in the models with pure normal dip-slip along the basal fault (Fig. 12), whereas the impact of basal fault kinematics is best highlighted by comparing those models involving standard layering and varying kinematics (oblique and strike-slip; Fig. 13).

5.1.1 Influence of model layering

In the sand-only case (i.e. reference Model A1, Figs. 5a–d, 12a, g–j), we observe the initial development of a reverse fault after 2.6 mm of basal fault slip, followed by a normal fault, both rooting at the contact between the basal fault and the sand layer. The presence of a reverse fault in such a basal normal fault model set-up may seem somewhat surprising, but has been observed in previous studies with very similar (sand-only) set-ups (e.g. Koopman et al., 1987; Naylor et al., 1994; Richard, 1989, 1991; Sanford, 1951; Schmatz et al., 2010; Withjack & Callaway, 2000; Withjack et al., 1990). In these studies, the authors found that vertical (i.e. 90° dipping) basal normal faults induce such combined reverse and normal faulting in the overlying sand layer, whereas shallowly dipping basal faults (45°) led to normal faulting only. Our model set-up, with its 75° basal fault inclination clearly falls in the steep

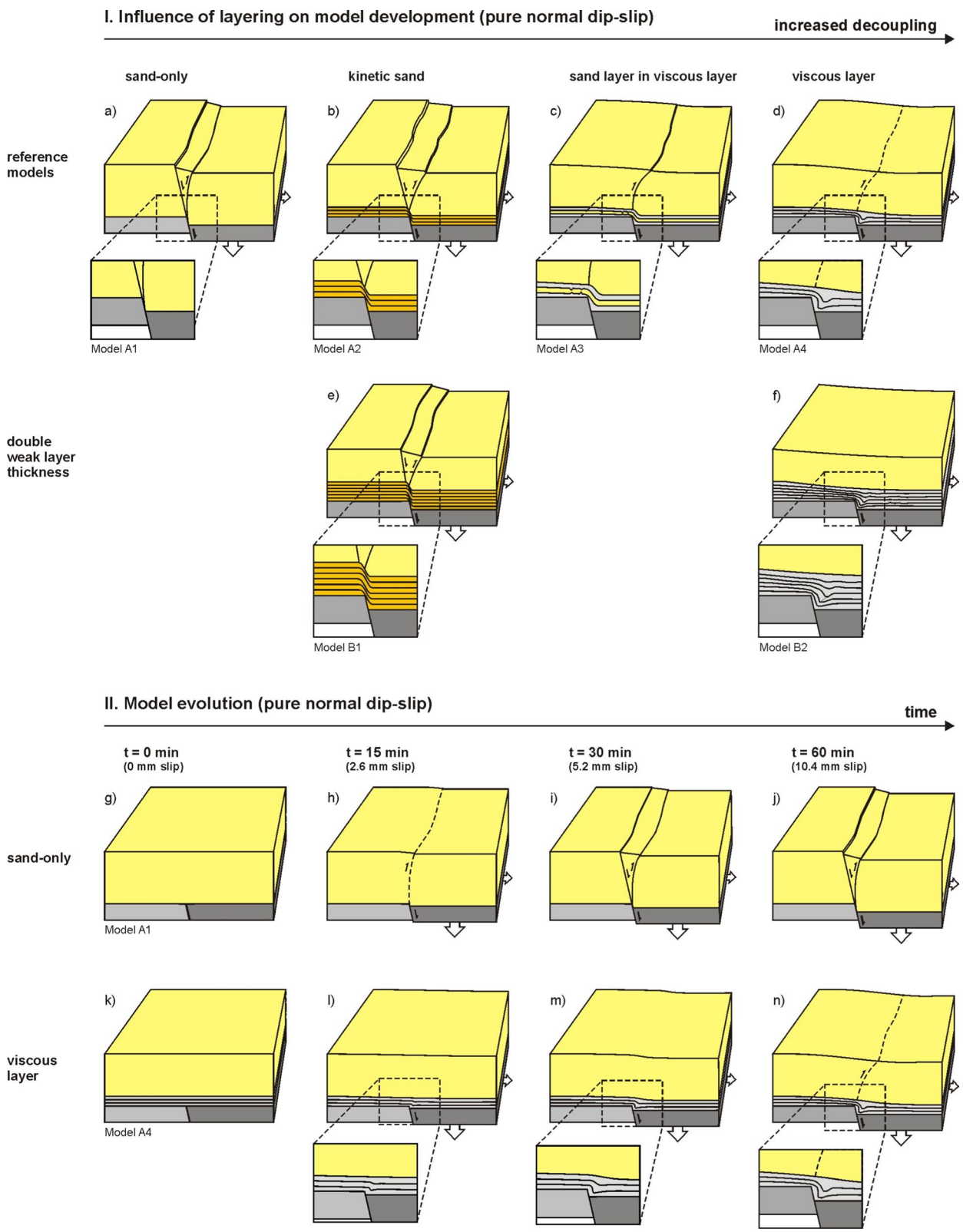

Fig. 12 Schematic overview depicting the influence of viscous layer properties on model development (in pure normal dip-slip models). **a**–**f** Final state of model deformation. **g**–**n** Evolution of **g**–**j**) sand-only Model A1, and **k**–**n** of Model A4 with a standard thickness viscous layer

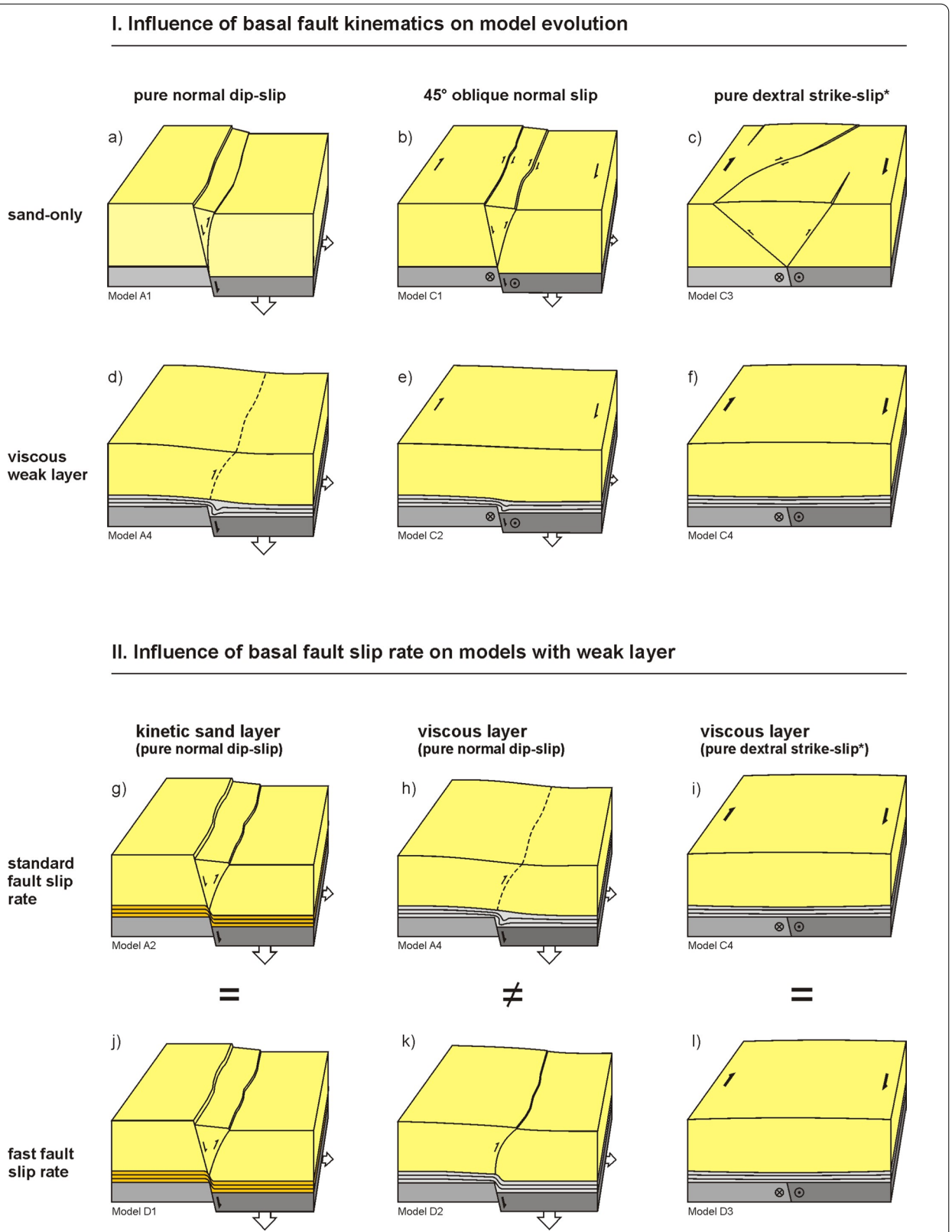

Fig. 13 Schematic overview depicting the influence of basal fault kinematics on model development (final model stage). *Pure dextral strike-slip results after double amounts of slip (compared to the pure normal dip-slip and 45° oblique normal slip models)

fault part of the spectrum (Withjack et al., 1990). The explanation for the initial development of reverse faulting above steep basal faults is that the maximum shear stress along the basal fault is also oriented vertically, which in combination with the resulting oblique orientation of the principal stress (σ_1) forces reverse faulting in the overburden (Roche et al., 2000).

However, when adding increasingly viscous basal layers to the models, the deformation style starts to change (Fig. 12b-d). Kinetic sand (as in Model A2, Fig. 5e–h, 12b) leads to some folding at the base of the model to compensate for the slip along the basal fault due to the visco-brittle properties of the kinetic sand, delaying the faulting in the sand. Yet the general model structure is very similar to that of the sand-only equivalent, with the exception that the faults are rooted at the interface between the kinetic sand and the sand overburden, rather than at the base of the model materials as in the sand-only case (Fig. 12a, b). At a later stage however, the fault crosses into the kinetic sand, indicating that the material undergoes only limited viscous flow before switching to a more brittle-style of deformation (Figs. 5h, 12b).

A layer of properly viscous material allows for even more compensation of basal fault slip by folding and viscous flow (Fig. 12c, d). In Model A3, which contains a sand layer within the viscous layer (Figs. 6a–d, 12c), the flow and folding of the viscous layer sufficiently compensate basal fault slip to only allow the delayed development of a reverse fault in the overlying sand layer (Fig. 6c). The boudinage affecting the sand layer within the viscous layer uniquely highlights the internal deformation (i.e. stretching) of the viscous material above the basal footwall, whereas internal deformation in the thin sand layer allows it to accommodate downward warping above the basal fault (similar to thin brittle overburden layers in Withjack & Callaway, 2000; Zwaan et al., 2020). Although boudinage has been studied in previous modelling studies (e.g. Mandal et al., 2007; Mengong & Zulauf, 2007; Passchier & Druguet, 2002; Zulauf et al., 2014), we are not aware of any study producing boudinage structures resulting from a similar model set-up as the one we apply. Perhaps the closest are the clay layers in the models by Schmatz et al. (2010).

The effects of viscous flow are even better visible when a purely viscous layer is applied (e.g. Model A4, Figs. 6e–h, 12d, k–n). Here, we see the gradual stretching and thinning of the viscous layer above the basal footwall block, the thickening of and folding within the viscous layer above the hanging wall block, and the flow of material down along the basal fault plane. As a result, the sand overburden is largely decoupled from the basal fault, so that the brittle overburden is passively tilted towards the basal hangingwall block, while only minor faulting in the sand is observed (Figs. 6e–h, 12d, k–n). Such decoupling effects due to the presence of a viscous layer are well known from various previous studies with similar set-ups (e.g. Dooley et al., 2003; Naylor et al., 1994; Richard, 1989, 1991; Schori et al., 2021; Withjack & Callaway, 2000), but the details of flow within the viscous layer has received limited attention so far. Dooley et al. (2017) propose the concept of "streamlines" based on an indirect analysis of viscous layer thicknesses in analogue models of salt tectonics to explain how viscous materials flow, and Brun and Beslier (1996) have included colour makers in their analogue models of lithospheric-scale rifting, allowing an impression of viscous flow at the end of the model run. Furthermore, Koyi (2001) and Dooley et al., (2009, 2015) have used marker layers in models of salt diapirs. To our knowledge, however, the use of marker layers within the viscous layer, combined with our progressive sectioning procedure, is unique and for the first time directly shows the complex evolution of layer-internal viscous flow in systems affected by basal faults, which would otherwise remain undetected.

It may be noted that by increasing the thickness of the viscous layer, the decoupling effects are enhanced so that the system is dominated by viscous flow and buffering of basal fault slip within the viscous layer (i.e. Model B2, Figs. 7e–h, 12e, Withjack & Callaway, 2000). As a result, no faulting is observed within the overlying sand layer. By contrast, the use of a thick kinetic sand layer does not prevent the development of similar structures as those in the equivalent model with a normal thickness kinetic sand layer (compare Models A2 and B1, Figs. 4e–h, 7a–d, 12b, e). However, also in the case of a thick kinetic sand layer, we find that faults tend to root at the interface of the kinetic sand layer and the sand overburden, so that the resulting fault structure is smaller in scale due to basic geometric relationships (fault inclinations and brittle layer thickness, see e.g. Allemand & Brun, 1991, and Zwaan et al., 2019).

5.1.2 Influence of basal fault kinematics

In addition to the presence and characteristics of a rheological weak layer, also the type of basal fault kinematics (i.e. slip direction and slip rate along the basal fault) has a pronounced effect on model evolution (Fig. 13). In fact, both layering and fault kinematics interact in various ways.

Firstly, the sand-only models show how pure normal dip-slip (in Model A1) creates the reverse and normal fault structures discussed in Sect. 5.1.1 (Figs. 12a, g–j, 13a). By contrast, the pure dextral strike-slip in Model C3 leads to the development of a pop-up structure with strike-slip component that is rooted at the basal velocity discontinuity (VD), with the boundary faults of this

pop-up structure crossing the model centre in a right-stepping en echelon fashion (Figs. 9a, d, i, j, 13c). Such structures are typical of strike-slip models (e.g. Dooley & Schreurs, 2012, and references therein), where it must be stressed that small deviations from pure strike-slip deformation may cause the system to either create transtensional or transpressional structures (e.g. Fedorik et al., 2019; Viola et al., 2004). Furthermore, there are no clear indications in section view that the model involves strike-slip deformation, as one could interpret the pop-up structure as a result of in-section contraction. It is also important to recognize that these structures only develop in response to large amounts of fault slip, showing that dip-slip is a more efficient means of inducing faulting in the overburden of the weak layer. This relatively large impact of the dip-slip component is clear from the 45° oblique normal slip model results (Model C1, Figs. 8a–d, 13b), which have no clear indications of the equally large strike-slip deformation component and as such closely resemble the pure normal dip slip model results (Fig. 13a), but at an earlier stage of development (compare Fig. 13b with Fig. 12i). Those insights highlight the importance of understanding the 3D evolution of tectonic structures and are very much in line with results from Richard (1989, 1991), who ran similar models and also registered the dominance of the dip-slip over the strike-slip component. However, the brittle-only models by Von Hagke et al. (2019) show that oblique normal slip can also cause the development of en echelon normal faulting overlying a basal fault. This may however be influenced by their set-up involving a 60° dipping normal fault and their use of a granular material with a higher cohesion than our quartz sand.

When a viscous weak layer is included, the decoupling involved strongly modifies the development of our models (Fig. 13d–f). As described in Sect. 5.1.1, deformation in pure normal dip-slip systems (i.e. Model A4, Fig. 5e–h) is buffered by viscous flow in the weak layer, so that only limited faulting appears in the overlying sand layer (Fig. 12d). In the case of pure dextral-strike slip (Model C4, Figs. 9e–h, k, l, 13f), no faulting is observed in the brittle layer. Instead, we observe a slight bulging of the sand layer, and a slight thinning of the weak layer below. However, even the larger amount of basal fault slip applied in this model does not create any obvious strike-slip related structures in either the viscous layer or the overlying sand cover. As with the pop-up in the sand-only equivalent (Fig. 13c), the bulging of the sand layer could be interpreted as a result of in-section contraction. Furthermore, similar to the sand-only case, the 45° oblique normal slip results (i.e. Model C2, Fig. 8e–h, Fig. 13e) very much resemble the structures of the pure normal dip-slip model (Fig. 13d), but in an earlier stage of development (i.e. prior to the appearance of faulting in the sand layer). At the same time, the structures do not seem to register any impact of the significant strike-slip component applied in the model. As with the sand-only models, these insights from our models with a viscous weak layer are very much in accordance with those from similar models in Richard (1989, 1991), again highlighting the dominance of dip-slip deformation along basal faults, and the importance of understanding the third dimension in such tectonic systems. It should however be pointed out that, similar to sand-only models (Von Hagke et al., 2019), other studies have also produced en echelon basins during oblique extension (Zwaan et al., 2020). However, instead of a basal fault, these authors used a viscous rheological contrast to generate differential subsidence. Still, also these model results may be relevant for interpreting natural examples.

Finally, basal fault slip rate has a secondary influence on the structural evolution of our models (Fig. 13g–l). Since sand behaviour is strain rate-independent under normal laboratory conditions, changing model strain rates is not expected to modify our model results, which are therefore not of interest here. In the case of kinetic sand Model D1 (Figs. 10a–d, 13j), the increased pure normal dip-slip rate does not provide a clear difference in model evolution (compare to model A2, Figs. 4e–h, 13g). This result highlights the significant brittle component of the kinetic sand rheology that was already apparent from the general resemblance to the pure sand equivalent (e.g. Fig. 13a). By contrast, when applying faster normal dip-slip to Model D2 with a viscous weak layer (Figs. 10e–h, 13k), the viscous material strengthens. As a result, the viscous layer cannot easily flow and compensate basal fault slip. Instead, it is dragged down with the basal hanging wall block, leading to increased faulting in the brittle overburden. This strengthening effect of viscous material subjected to increased strain rates, and the resulting coupling and transfer of deformation from the model base into the brittle overburden is well-known from previous modelling work (e.g. Brun, 1999; Withjack & Callaway, 2000; Zwaan et al., 2019). However, such enhanced enhanced transfer of deformation from the model base into the overburden is not observed in our fast strike-slip Model D3 (Figs. 11, 13i, l), once more highlighting the relatively minor impact of strike-slip displacement along basal faults on deformation in the overburden, and the need to understand tectonic systems in 3D.

5.2 Application of model results: comparison to natural examples

5.2.1 Zürcher Weinland

We first compare our model results to two selected structures in the Zürcher Weinland area: the Rafz-Marthalen

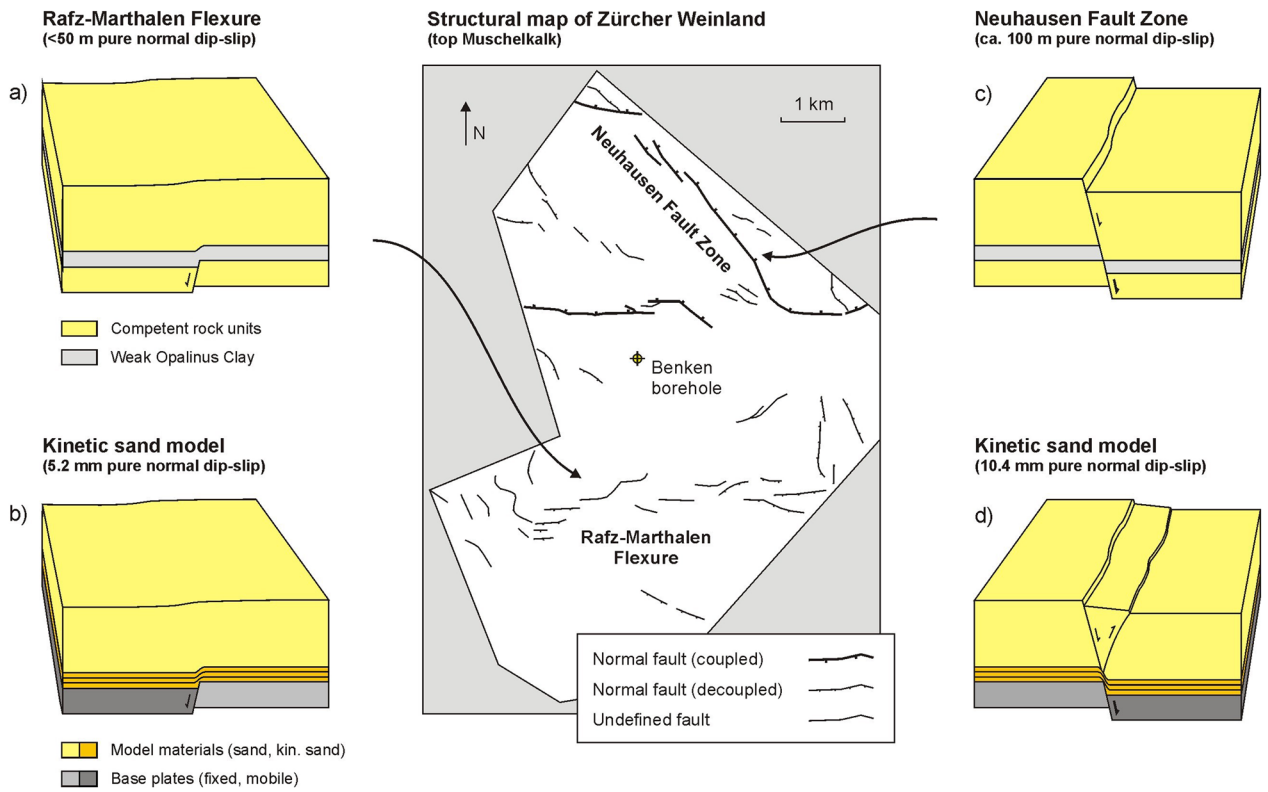

Fig. 14 Comparison of seismically mapped structures in the Zürcher Weinland region (compare Fig. 1b for location) redrawn in 3D after Roche et al. (2020) and our analogue model results. Middle: Structural map at Top Muschelkalk level, i.e. the top of the brittle sequence underlying the Opalinus Clay. **a**–**d** 3D sketches of the natural examples and respective analogue models from this study. **a**, **b** comparison of the Rafz-Marthalen Flexure (RMF). **c**, **d** Comparison of Neuhausen Fault (NHF). Scaling in our models: 10 mm in the model = 100 m in nature

Flexure (RMF) and the Neuhausen Fault Zone (NFZ) (Figs. 1c, 2a, c, 14). In the case of the RMF, motion along the various basal faults, although likely related to reactivation of Late Paleozoic precursor structures during the Late Oligocene/Early Miocene formation of the Swiss Molasse Basin (Birkhäuser et al., 2001; Malz et al., 2016), did not result in propagation of faulting into the overburden (Fig. 14a). This lack of faulting in the overburden is most likely due to the relatively minor normal dip slip along the individual basal faults (< 50 m). This is in accordance with our (Model A2) results, which suggest that, even considering the Opalinus Clay to be relatively competent (as simulated by a kinetic sand layer), more than over 50 m of deformation would be needed before faulting would initiate in the overburden (Figs. 12b, 14b).

The NW–SE striking Neuhausen Fault Zone (NHFZ) relates to the formation of the Middle Miocene Hegau-Lake Constance Graben (Birkhäuser et al., 2001; Egli et al., 2017; Fig. 1c). The NHFZ is characterized by up to 100 m pure normal dip slip accumulated along the basal fault in Miocene times (Birkhäuser et al., 2001; Egli et al., 2017; Madritsch, 2015; Roche et al., 2020). As constrained by seismic data, the steep basal fault has propagated upward through the Opalinus Clay, into the overburden, apparently in the form of a single steep normal fault (Figs. 2c, 14c). Comparing our model results to the NHF, we find that the model with a kinetic sand layer after 10 mm (100 m) pure normal dip-slip provides the best fit, even though we do not observe the model's reverse faulting in the natural case (Fig. 14c, d). Since the basal fault dip in nature is the same as in our models (ca. 75°), the reverse faulting may be an artefact of the relatively low cohesion in our model quartz sand layers (see Sect. 3.5 on scaling, and the models by Von Hagke et al., 2019). Alternatively, a minor component of reverse faulting (< < 20 m) may just not be resolvable by seismic data.

Overall, the comparison between our models with deformation structures in the "Zürcher Weinland" suggests that the > 100 m thick weak layer represented by the Opalinus Clay appears to have a strong buffering effect on "basal faults" with smaller vertical offsets. Indeed, fault propagation across the Opalinus Clay requires relatively strong tectonic deformation, i.e. fault displacement > 50 m. This is in accordance with data from past

and recent boreholes (Nagra, 2001, 2022; Roche et al., 2020) that show very limited faulting within the Opalinus Clay.

5.2.2 Wider Swiss Alpine Foreland

Even though layer thicknesses of the brittle overburden of the Middle Jurassic weak layer change considerably in the wider Swiss Alpine Foreland when moving away from the Zürcher Weinland (both towards the Alpine front and towards the SW), some additional structures from this area can also be interpreted using our model results.

Firstly, we focus on the St. Gallen Fault Zone (SGFZ), which involves reactivation of a Permo-Carboniferous trough-bounding fault zone that has been active up to the present day (Diehl et al., 2017; Fabbri et al., 2021; Heuberger et al., 2016; Fig. 15a). In section view the SGFZ shows both normal faulting and reverse faulting, with > 100 m basal fault normal dip-slip affecting the Mesozoic sediments overlying the Permo-Carboniferous trough (Fig. 15a. No clear signs of decoupling along the Opalinus Clay, or any other weak layer that may be present in the area (e.g. Triassic evaporites, Fig. 2c) is

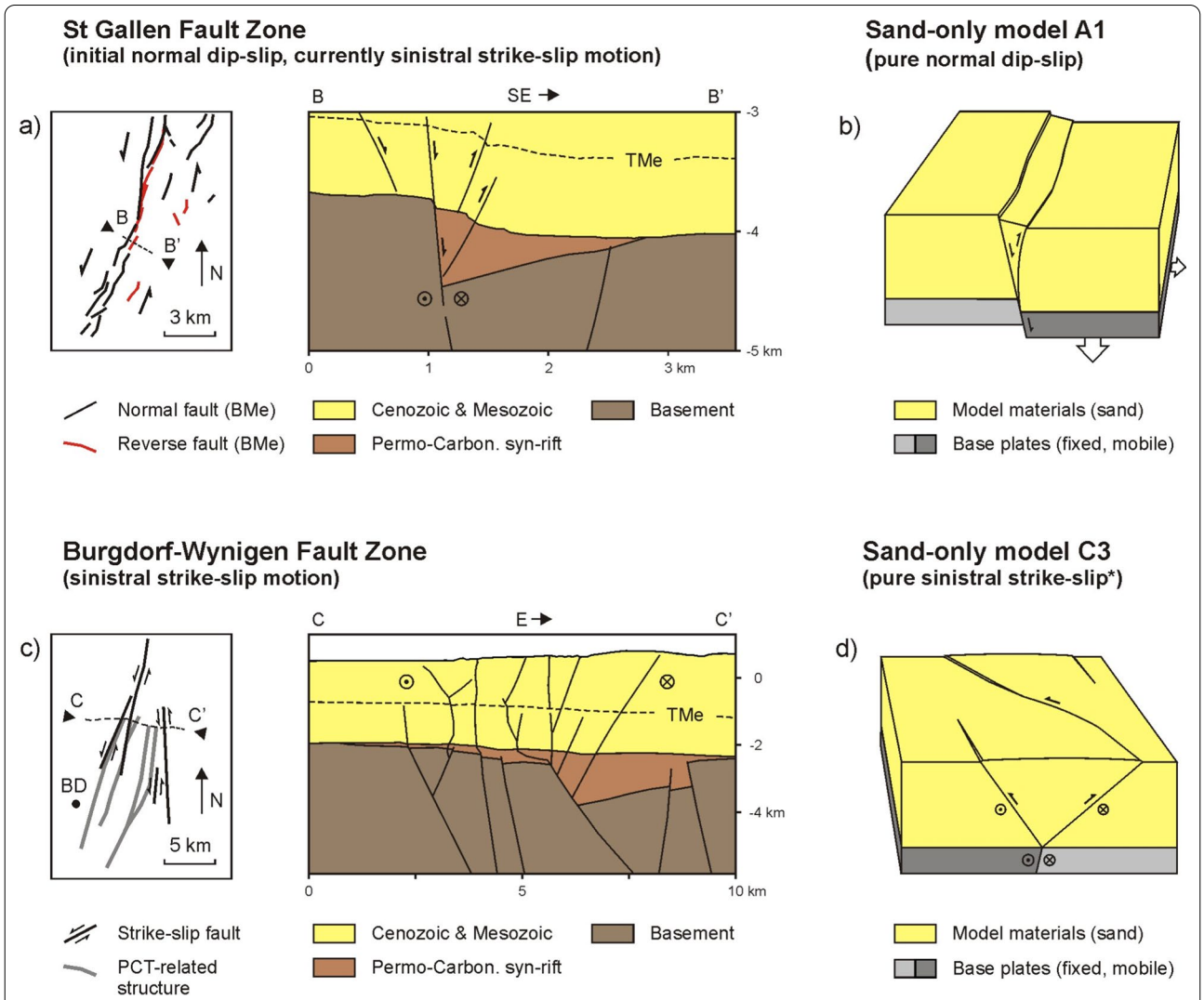

Fig. 15 Comparison of structures from the wider Swiss Alpine Foreland with analogue model results. **a** Simplified map and section view of the Sankt Gallen Fault Zone (normal dip-slip fault, reactivated as a sinistral strike-slip fault), compared to **b** our sand-only pure normal dip-slip model A1. Redrawn after Diehl et al. (2017), based on data from Heuberger et al. (2016). **c** Simplified map and section view of the Burgdorf-Wynigen Fault Zone (sinistral strike-slip kinematics), compared to **d** our sand-only pure strike-slip model C3. *The original dextral-strike-slip model is mirrored to reflect the natural situation. Redrawn after Mock and Herwegh (2017). *BD* Burgdorf. *PCT* Permo-Carboniferous Trough, *BMe* Base Mesozoic, *TMe* Top Mesozoic. Locations of the St Gallen Fault Zone and the Burgdorf-Wynigen Fault Zone are indicated in Fig. 1b

observed. As such, the SGFZ structure is very similar to our sand-only normal dip-slip model Model A1 without a weak layer (Figs. 4a–d, 12a, g–j). However, focal mechanisms along the SGFZ indicate on-going sinistral strike-slip deformation, rather than normal dip-slip motion (Diehl et al., 2017; Heuberger et al., 2016). These observations highlight the polyphase evolution of the SGFZ, with initial periods of Mesozoic to Oligocene dip-slip motion along the pre-existing basal fault causing the pronounced normal and reverse faulting found in the Mesozoic / Cenozoic units (Fig. 15b), whereas the currently active strike-slip motion results from the present-day stress field (Heuberger et al., 2016). Importantly, compared to the Zürcher Weinland where the Opalinus Clay caused considerable decoupling, the high degree of coupling along the SGFZ is likely due to the much thicker overburden (> 3000 m, versus 530 m in the Zürcher Weinland, Figs. 2b, c, 15a). A thicker overburden is indeed known to significantly decrease the decoupling influence of weak layers (Withjack & Callaway, 2000), and this effect is also apparent in our models (Fig. 12d, f).

Increased coupling due to a thicker overburden is also observed along the Burgdorf-Wynigen Fault Zone (BWFZ) located in the central, thrusted part of the Swiss Alpine foreland (Figs. 1b, 15c). The BWFZ is characterized by currently active sinistral strike-slip deformation along a reactivated normal fault zone bounding a Permo-Carboniferous trough (Mock & Herwegh, 2017, Fig. 15c). Also here, rheological weak layers such as the Opalinus Clay or weak Triassic evaporites are thicker than in the Zürcher Weinland, but do not seem to significantly reduce coupling. The structures in our models and in nature are not very similar at first sight, probably due to the complexity of the inherited deep structure of the BWFZ (Fig. 15c, d). However, what our model results do suggest is that considering the lack of a significant dip-slip component, Miocene to recent strike-slip displacement along the BWFZ must have been considerable (i.e. several hundreds of meters) to allow for the development of clear strike-slip faults in the upper Mesozoic and Cenozoic sedimentary sequence (Mock & Herwegh, 2017, Figs. 9a–d, 15c, d). This need for large strike-slip displacements in order to create structures in the overburden implies that there may be other, smaller "blind" strike-slip faults in the area that did not (yet) accommodate sufficient displacement to significantly affect the overburden. Nevertheless, also such smaller strike-slip faults could be relevant in the context of seismic hazard assessment (see also Sect. 5.2.3).

5.2.3 Broader application of our model results

Apart from the comparisons with fault zone examples from the Swiss Alpine Foreland, our model results are also of use for interpreting structures from elsewhere around the world. For instance, the relationship between the thickness and rheology of a weak layer and decoupling between deformation below and above the layer (Fig. 13) is observed at various locations (Ferrill & Morris, 2008; Ferrill et al., 2017). In the North Sea, Permian Zechstein salt caused decoupling of overburden from normal faulting along reactivated basement faults (e.g. Stewart, 2007; Stewart & Clark, 1999; Warsitzka et al., 2021; Fig. 16a), favouring the development of monoclines in the weak layer overburden, similar to what we see in our models (e.g. Ferrill et al., 2007) (Figs. 12d, f, k–n, 13e, h). Other examples can be found in the Bresse Graben (France, Fig. 1a), where Triassic Salt forms a weak pre-rift layer (Rocher et al., 2003), and at various locations

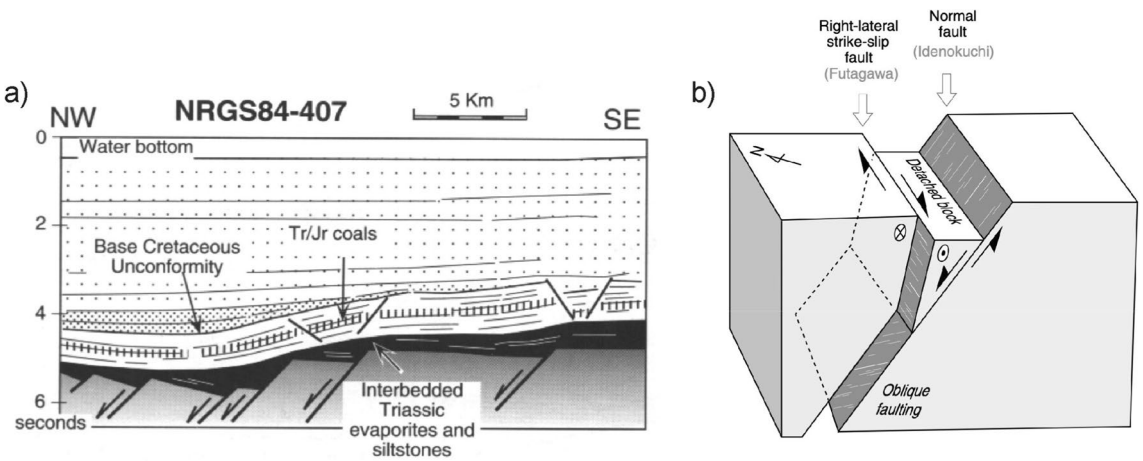

Fig. 16 **a** Line drawing of time-migrated seismic section (NRGS84-407) across the Smørbukk structure, Norwegian North Sea (modified after Withjack et al., 1990). AAPG ©1990, reprinted by permission of the AAPG whose permission is required for further use. **b** Sketch of slip partitioning that occurred during the 2016 Kumamoto earthquake. Modified after Toda et al. (2016)

in Texas (USA), where clay-rich shales form weak layers above basal faults (Ferrill & Morris, 2008; Ferrill et al., 2004, 2007).

Furthermore, the novel direct observations of internal deformation within the weak layers of our models appears to be especially relevant for other tectonic settings. They reveal much more complex flow patterns than would be expected otherwise (Figs. 12c, d, f, k–n, 13d–e, h, k). This is reminiscent of the complex internal flow of salt diapirs (e.g. Jackson & Talbot, 1986), and viscous materials similar to those in our models are indeed used for the simulation of salt tectonics in many analogue modelling studies (e.g. Fort et al., 2004a, 2004b; Warsitzka et al., 2021; Zwaan et al., 2021b). Our model results show that even though a weak layer may seem relatively undisturbed at first sight, significant internal deformation may have taken place nevertheless, and needs to be taken into account for a proper understanding of the system. Such internal deformation is especially relevant when weak layers are considered for their georesource potential (e.g. for salt production or gas storage), where the presence and distribution of impurities and heterogeneities poses significant challenges (e.g. Duffy et al., in review; Jackson & Hudec, 2017; Rowan et al., 2019; Strozyk et al., 2012; Warren, 2016).

Other important general insights derived from our models regard the structural expression of strike-slip deformation. Whereas our model results suggest that basal fault dip-slip motion can have a strong imprint on deformation in the weak layer overburden, even during an early deformation stage, strike-slip deformation along the basal fault needs to be significant to lead to a discernibly imprint in the weak layer overburden (Figs. 12, 13). As such, apparent normal fault structures may very well conceal an important strike-slip deformation component, as shown to be present in our oblique-slip models (Fig. 13b). In fact, such apparent normal fault systems that effectively accommodate oblique-slip deformation are reported on the island of Kyushu (Japan) (Fig. 14b), and in Central Nevada and the Walker Lane fault system (USA) (Caskey et al., 1996; Toda et al., 2016; Wesnousky, 2005), with implications for local earthquake risk assessment. Pure strike-slip systems can be even more challenging to assess since our models illustrate that such systems may undergo strike-slip deformation without readily detectable surface expression (Figs. 9, 11, 13f, i, l). Some natural examples are the blind strike-slip fault near the town of Bam in Iran (Talebian et al., 2004) the Andravida fault in Greece (Karakonstantis et al., 2019), and various seismically active structures in the California Continental Borderland, USA.

These results and considerations again highlight the need for a thorough 3D understanding of tectonic structures, since (minor) strike-slip deformation components in fault zones can otherwise be easily overlooked.

6 Conclusion

In this study we use a series of analogue models, inspired by the geology of the Zürcher Weinland region in the Northern Alpine Foreland Basin, to determine the influence of rheologically weak (partially ductile) layers and basal fault kinematics on the 3D evolution of deformation in the weak layer overburden and, uniquely, within the weak layer itself. Our model results lead us to the following conclusions:

- A weak layer is capable of decoupling the weak layer's overburden from deformation along the basal (normal) fault below it, so that the overburden deforms in a different manner than the basal fault does. This decoupling effect is enhanced by decreasing the strength of the materials comprising the weak layer, or by increasing the weak layer's thickness. By contrast, increasing the amount of basal fault slip, or increasing basal fault slip rate enhances coupling, so that deformation is more readily transferred from the basal fault into the overburden.
- Our models suggest that normal dip-slip motion, rather than strike-slip motion along the basal fault leads to deformation in the overburden of the weak layer in the case of low to intermediate displacements. Whereas the interaction between these slip components may sometimes be complex, especially when basal fault dip and cohesion of the overburden are taken into account, relatively small magnitudes of normal dip-slip can lead to overburden deformation. By contrast, it appears that larger magnitudes of strike-slip displacements are required to achieve recognizable deformation in the overburden. As a result, strike-slip components can easily be overlooked, with implications for seismic risk assessment, and may only be revealed when 3D fault analysis is applied.
- When comparing our model results to natural examples we find a fair fit; our model results explain various features of the structures found in the (Swiss part of) the Northern Alpine Foreland Basin, and suggest that weak layers such as the Middle Jurassic Opalinus Clay have exerted significant control on fault zone architecture.
- Furthermore, the novel addition of internal marker layers to the weak layer, in combination with our progressive sectioning method, reveals that when the system is sufficiently weak, the basal fault slip can to a large degree be accommodated by complex viscous flow within the weak layer. This viscous flow would otherwise go unnoticed, but may be of great signifi-

cance for understanding the tectonic history of certain fault systems, and in cases where weak layers are being considered as potential georessource (e.g. salt mining).

The above results demonstrate the complex links between fault kinematics, mechanics and 3D geometries. Profound knowledge of the temporal evolution of these links in nature is of great importance. As such we consider our models a useful analogue not only for the northern Alpine foreland basin but also for other regions featuring similar tectonic / structural settings.

Appendix

Model preparation

All model materials are built into the general set-up consisting of sidewalls and base plates (Fig. 3), which are covered with a sub-millimetre thick plastic foil ("Alkor" foil 120,010 formerly produced by Alkor-Venilia, now available as "Gekkofix 11,325" http://www.gekkofix.com, Klinkmüller et al., 2016). The angle of boundary friction of the foil with quartz sand lies between 15° and 21° (Schreurs et al., 2016). Subsequently, the model materials are added on top of this set-up.

Sand is simply sieved into the model (i.e. onto the detachment layer, or onto the model base) from a heigh ≥ 30 cm to ensure a constant density (e.g. Klinkmüller et al., 2016; Schmid et al., 2020). It is regularly flattened by means of a scraper. At these scraping intervals (of 4 mm in the lower 1.2 cm of the model, and of 1 cm in the overlying material), we apply (sieve in) a thin (< 1 m) marker layer of dark corundum sand that allows the tracing of internal deformation on cross-sections (Sect. 3.5). This dark corundum sand has very similar properties to the quartz sand (Table 1), and its presence (or the regular scraping) is not expected to significantly affect model results.

The kinetic sand is applied in a different manner than the quartz sand since it cannot simply be sieved into the model. Instead, we apply a manual roller pin method to prepare layers of kinetic sand of ca. 4 mm thickness each, which are subsequently added to the model. Similarly to the quartz sand, we insert (sieve in) thin (< 1 mm) marker intervals within the individual 4 mm kinetic sand layers to trace deformation on cross-sections. Since the kinetic sand is darker than the quartz sand, we use the white FS900F feldspar sand for the marker layers instead. The presence of these thin marker layers is not considered to significantly affect model evolution. Note that, since the prepared kinetic sand layers do not cover the whole width of the model, we use feldspar sand to fill in any gaps that may occur along the sidewalls. This filling of gaps with feldspar sand does not cause any observable boundary effects.

The basic method used for creating the viscous layers is similar to the method used for the kinetic sand, with the difference that we use a KitchenAid® mixer with pasta attachment to create thin layers (manually rolling the material being impractical) that are subsequently added to the model. Also in the dark viscous mixture, we create (sieve in) thin (< 1 mm) marker intervals with white feldspar sand at 4 mm layer thickness intervals, and any gaps along the sidewalls are filled with feldspar sand as well. Similar to the models with a kinetic sand detachment, the use of feldspar sand for creating marker layers and filling gaps does not cause clear boundary effects. In the case of Model A3, the central 4 mm of viscous mixture is replaced by an equally thick layer of quartz sand that is simply sieved in.

While preparing the model, a sand talus develops on both short ends of the model since for practical reasons no confinement is present there (Fig. 3a). This sand talus then serves as model confinement, which is important to prevent the detachment layer materials from flowing sideward. Previous modelling efforts (e.g. Zwaan et al., 2021a, 2022a) have shown the effectiveness of this type of model confinement, and only very limited boundary effects occur.

Finally, after the general model layer cake is completed, a 4×4 grid of dark corundum sand (< 1 mm thick) is added to the model surface, as is a pattern of coffee powder (Fig. 4a). These measures help for subsequent model analysis (Sect. 3.5).

Acknowledgements

We thank our colleagues from GFZ Potsdam and from the University of Montpellier for discussing the properties of the kinetic sand, and for performing its rheological characterization. Kirsten Elger and Florian Ott helped us prepare the GFZ data publication containing the supplementary material linked to this paper (Zwaan et al. 2022b). Raphael Schneeberger provided valuable feedback and ensured smooth communication with the project funder (Nagra). We furthermore thank Adam Cawood, Vincent Roche, and an anonymous reviewer for their constructive commentary that helped improving the manuscript, and we thank editors Daniel Marty and Stefan Schmid for efficiently guiding the review process.

Author contributions

All authors were involved in the conception of the research project. FZ and GS designed the analogue model series, and funding was secured by HM (based on a proposal written by GS and FZ, with input from HM and MH). FZ completed the model series, performed the analysis of the model results, and drafted the text of the manuscript, with regular input from the other authors. All authors read and approved the final manuscript.

Funding

This work was funded by the National Cooperative for the Disposal of Radioactive Waste (Nagra) in Switzerland, who also covered the Open Acces publication costs. FZ was furthermore supported by a 2022 GFZ Discovery Fellowship grant.

Availability of data and materials
The dataset supporting the conclusions of this article (overview figures and videos of model results) is publicly available at GFZ Data Services (Zwaan et al., 2022b, https://doi.org/10.5880/fidgeo.2022.032).

Declarations

Ethics approval and consent to participate
Yes.

Consent for publication
Yes.

Competing interests
The authors declare that they have no competing interests.

Author details
[1]Institute of Geological Sciences, University of Bern, Baltzerstrasse 1+3, 3012 Bern, Switzerland. [2]Helmholtz Centre Potsdam-GFZ German Research Centre for Geosciences, Telegrafenberg, 14473 Potsdam, Germany. [3]National Cooperative for the Disposal of Radioactive Waste (Nagra), Hardstrasse 73, 5430 Wettingen, Switzerland.

Received: 25 July 2022 Accepted: 5 November 2022
Published online: 16 December 2022

References

Allemand, P., & Brun, J.-P. (1991). Width of continental rifts and rheological layering of the lithosphere. *Tectonophysics, 188*, 63–69. https://doi.org/10.1016/0040-1951(91)90314-I

Allenbach, R., Baumberger, R., Kurmann, E., Micahel, C.S., & Reynolds, L. (2017). GeoMol: Geologisches 3D-Modell des Schweizer Molassebeckens: Schlussbericht, Swisstopo, Wabern. https://www.swisstopo.admin.ch/en/knowledge-facts/geology/geological-data/3d-geology/deep/geomol.html

Amann, F., Wild, K. M., Loew, S., Yong, S., Thoeny, R., & Frank, E. (2017). Geomechanical behaviour of Opalinus Clay at multiple scales: Results from Mont Terri rock laboratory (Switzerland). *Swiss Journal of Geosciences, 110*, 151–171. https://doi.org/10.1007/s00015-016-0245-0

Birkhäuser, P., Roth, P., Meier, B. & Naef, H. (2001). 3D-Seismik: Räumliche Erkundung der mesozoischen Sedimentschichten im Zürcher Weinland. Nagra Technical Report, NTB 00-03. Nagra, Wettingen. https://nagra.ch/downloads/technischer-bericht-ntb-00-03/

Bläsi, H. R., Deplazes, G., Schnellmann, M. & Traber, D. (2013). Sedimentologie und Stratigraphie des ‹Braunen Doggers› und seiner westlichen Äquivalente. Nagra working report, NAB 12—51. Nagra, Wettingen. https://nagra.ch/en/downloads/arbeitsbericht-nab-12-51-2/

Brun, J.-P. (1999). Narrow rifts versus wide rifts: Inferences for the mechanics of rifting from laboratory experiments. *Philosophical Transactions: Mathematical, Physical and Engineering Sciences, 357*, 695–712. http://www.jstor.org/stable/55066

Brun, J. P., & Beslier, M. O. (1996). Mantle exhumation at passive margins. *Earth and Planetary Science Letters, 142*, 161–173. https://doi.org/10.1016/0012-821X(96)00080-5

Burkhard, M. (1990). Aspects of the large-scale Miocene deformation in the most external part of the swiss Alps (subalpine Molasse to Jura fold belt). *Eclogae Geologicae Helvetiae, 83*, 559–583. https://doi.org/10.5169/seals-166602

Burliga, S., Koyi, H. A., & Chemia, Z. (2012). Analogue and numerical modelling of salt supply to a diapiric structure rising above an active basement fault. *Geological Society, London, Special Publications, 363*, 395–408. https://doi.org/10.1144/SP363.18

Byerlee, J. (1978). Friction of rocks. *Pure and Applied Geosphysics, 116*, 615–626. https://doi.org/10.1007/BF00876528

Caskey, S. J., Wesnousky, S. G., Zhang, P., & Slemmons, D. B. (1996). Surface Faulting of the 1954 Fairview Peak (M_S 7.2) and Dixie Valley (M_S 6.8) Earthquakes, Central Nevada. *Bulletin of the Seismological Society of America, 86*, 761–787. https://doi.org/10.1785/BSSA0860030761

Cederbom, C. E., van der Beek, P., Schlunegger, F., Sinclair, H. D., & Oncken, O. (2011). Rapid extensive erosion of the North Alpine foreland basin at 5–4 Ma. *Basin Research, 23*, 528–550. https://doi.org/10.1111/j.1365-2117.2011.00501.x

Childs, C., Nicol, A., Walsh, J. J., & Watterson, J. (1996). Growth of vertically segmented normal faults. *Journal of Structural Geology, 18*, 1389–1397. https://doi.org/10.1016/S0191-8141(96)00060-0

Dèzes, P., Schmid, S. M., & Ziegler, P. A. (2004). Evolution of the European Cenozoic Rift System: Interaction of the Alpine and Pyrenean orogens with their foreland lithosphere. *Tectonophysics, 389*, 1–33. https://doi.org/10.1016/j.tecto.2004.06.011

Diebold, P., Naef, H., Ammann, M. (1991). Zur Tektonik der zentralen Nordschweiz. Interpretation aufgrund regionaler Seismik, Oberflächengeologie und Tiefbohrungen. Nagra Technical Report, NTB 90–04. Wettingen: Nagra. https://nagra.ch/downloads/technischer-bericht-ntb-90-04/

Diebold, P., & Noack, T. (1997). Late Palaeozoic troughs and Tertiary structures in the eastern folded Jura. In O. A. Pfiffner, P. Lehner, & P. Heitzmann (Eds.), *Deep structure of the Swiss Alps: results of NRP 20* (pp. 59–63). Birkhäuser.

Diehl, T., Clinton, J., Cauzzi, C., Kraft, T., Kästli, P., Deichmann, N., Massin, F., Grigoli, F., Molinari, I., Böse, M., Hobiger, M., Haslinger, F., Fäh, D., & Wiemer, S. (2021). Earthquakes in Switzerland and surrounding regions during 2017 and 2018. *Swiss Journal of Geosciences, 114*, 4. https://doi.org/10.1186/s00015-020-00382-2

Diehl, T., Deichmann, N., Clinton, J., Kästli, P., Cauzzi, C., Kraft, T., Behr, Y., Edwards, B., Guilhelm, A., Korger, E., Hobiger, M., Haslinger, F., Fäh, D., & Wiemer, S. (2015). Earthquakes in Switzerland and surrounding regions during 2014. *Swiss Journal of Geosciences, 108*, 425–443. https://doi.org/10.1007/s00015-015-0204-1

Diehl, T., Kraft, T., Kissling, E., & Wiemer, S. (2017). The induced earthquake sequence related to the St. Gallen deep geothermal project (Switzerland): Fault reactivation and fluid interactions imaged by microseismicity. *Journal of Geophysical Research: Solid Earth, 122*, 7272–7290. https://doi.org/10.1002/2017JB014473

Dooley, T., Hudec, M. R., Carruthers, D., Jackson, M. P. A., & Luo, G. (2017). The effects of base-salt relief on salt flow and suprasalt deformation patterns—Part 1: Flow across simple steps in the base of salt. *Interpretation, 5*, SD1–SD23. https://doi.org/10.1190/INT-2016-0087.1

Dooley, T., McClay, K. R., & Pascoe, R. (2003). 3D analogue models of variable displacement extensional faults: Applications to the Revfallet Fault system, offshore mid-Norway. *Geological Society, London, Special Publications, 212*, 151–167. https://doi.org/10.1144/GSL.SP.2003.212.01.10

Dooley, T., & Schreurs, G. (2012). Analogue modelling of intraplate strike-slip tectonics : A review and new experimental results. *Tectonophysics, 574–575*, 1–71. https://doi.org/10.1016/j.tecto.2012.05.030

Dooley, T. P., Jackson, M. P. A., & Hudec, M. R. (2009). Inflation and deflation of deeply buried salt stocks during lateral shortening. *Journal of Structural Geology, 31*, 582–600. https://doi.org/10.1016/j.jsg.2009.03.013

Dooley, T. P., Jackson, M. P. A., Jackson, C.A.-L., Hudec, M. R., & Rodriguez, C. R. (2015). Enigmatic structures within salt walls of the Santos BasindPart 2: Mechanical explanation from physical modelling. *Journal of Structural Geology, 75*, 163–187. https://doi.org/10.1016/j.jsg.2015.01.009

Duffy, O.B., Hudec, M.R., Peel, F., Apps, G., Bump, A., Moscadeli, L., Dooley, T.P., Bhattacharya, S., Wisian, K., & Shuster, M.W. (in review). The role of salt tectonics in the energy transition: An overview and future challenges. *Tektonika.*

Echtler, H. E., & Chauvet, A. (1992). Carboniferous convergence and subsequent crustal extension in the southern Schwarzwald (SW Germany). *Geodinamica Acta, 5*, 37–49. https://doi.org/10.1080/09853111.1992.11105218

Egli, D., Mosar, J., Ibele, T., & Madritsch, H. (2017). The role of precursory structures on Tertiary deformation in the Black Forest-Hegau region. *International Journal of Earth Sciences, 106*, 2297–2318. https://doi.org/10.1007/s00531-016-1427-8

Eisbacher, G. H., Lüschen, E., & Wickert, F. (1989). Crustal-scale trhursting and extension in the Hercynian Schwarzwald and Vosges, Central Europe. *Tectonics, 8*, 1–21. https://doi.org/10.1029/TC008i001p00001

Fabbri, S. C., Affentranger, C., Krastel, S., Lindhorst, K., Wessels, M., Madritsch, H., Allenbach, R., Herwegh, M., Heuberger, S., Wielandt-Schuster, U., Pomella, H., Schwestermann, T., & Anselmetti, F. S. (2021). Active Faulting in Lake Constance (Austria, Germany, Switzerland) unraveled

by multi-vintage reflection seismic data. *Frontiers in Earth Science, 9*, 670532. https://doi.org/10.3389/feart.2021.670532
Fedorik, J., Zwaan, F., Schreurs, G., Toscani, G., Bonini, L., & Seno, S. (2019). The interaction between strike-slip dominated fault zones and thrust belt structures: Insights from 4D analogue models. *Journal of Structural Geology, 122*, 89–105. https://doi.org/10.1016/j.jsg.2019.02.010
Ferrill, D. A., & Morris, A. P. (2008). Fault zone deformation controlled by carbonate mechanical stratigraphy, Balcones fault system, Texas. *AAPG Bulletin, 92*, 359–380. https://doi.org/10.1306/10290707066
Ferrill, D. A., Morris, A. P., McGinnis, R. N., Smart, K. J., Wigginton, S. S., & Hill, N. J. (2017). Mechanical stratigraphy and normal faulting. *Journal of Structural Geology, 94*, 275–302. https://doi.org/10.1016/j.jsg.2016.11.010
Ferrill, D. A., Morris, A. P., & Smart, K. J. (2007). Stratigraphic control on extensional fault propagation folding: Big Brushy Canyon monocline, Sierra Del Carmen, Texas. *Geological Society, London, Special Publications, 292*, 203–217. https://doi.org/10.1144/SP292.12
Ferrill, D. A., Sims, D. W., Waiting, D. J., Morris, A. P., Franklin, N., & Schultz, A. L. (2004). Structural framework of the Edwards Aquifer recharge zone in south-central Texas. *SGA Bulletin, 116*, 407–418. https://doi.org/10.1130/B25174.1
Fort, X., Brun, J. P., & Chauvel, F. (2004a). Contraction induced by block rotation above salt (Angolan margin). *Marine and Petroleum Geology, 21*, 1281–1294. https://doi.org/10.1016/j.marpetgeo.2004.09.006
Fort, X., Brun, J. P., & Chauvel, F. (2004b). Salt tectonics on the Angolan margin, synsedimentary deformation processes. *AAPG Bulletin, 88*, 1523–1544. https://doi.org/10.1306/06010403012
Giger, S. & Marschall, P. (2014). Geomechanical properties, rock models and in-situ stress conditions for Opalinus Clay in Northern Switzerland. Nagra Working Report, NAB 14-01. Nagra, Wettingen. https://nagra.ch/downloads/arbeitsbericht-nab-14-01/
Gruber, M. (2017). Structural investigations of the Western Swiss molasse basin: from 2D seismic interpretation to a 3D geological model. PhD Thesis. University of Fribourg, Switzerland.
Heuberger, S., Roht, P., Zingg, O., Naef, H., & Meier, B. P. (2016). The St. Gallen Fault Zone: A long-lived, multiphase structure in the North Alpine Foreland Basin revealed by 3D seismic data. *Swiss Journal of Geosciences, 109*, 83–102. https://doi.org/10.1007/s00015-016-0208-5
Hinsken, S., Ustaszewski, K., & Wetzel, A. (2007). Graben width controlling syn-rift sedimentation: The Palaeogene southern Upper Rhine Graben as an example. *International Journal of Earth Sciences (geologische Rundschau), 96*, 979–1002. https://doi.org/10.1007/s00531-006-0162-y
Hostettler, B., Reisdorf, A. G., Jaeggi, D., Deplazes, G., Bläsi, H., Morard, A., Feist-Burkhardt, S., Waltschew, A., Dietze, V., & Menfveld-Gfeller, U. (2017). Litho- and biostratigraphy of the Opalinus Clay and bounding formations in the Mont Terri rock laboratory (Switzerland). *Swiss Journal of Geosciences, 110*, 23–37. https://doi.org/10.1007/s00015-016-0250-3
Hubbert, M. K. (1937). Theory of scale models as applied to the study of geologic structures. *Geological Society of America Bulletin, 48*, 1459–1520. https://doi.org/10.1130/GSAB-48-1459
Ibele, T. (2015). Tectonics of the Hegau and Lake Constance Region: A synthesis based on existing Literature. Nagra Working Report, NAB 12–23, Wettingen, Nagra. https://www.researchgate.net/publication/347517161_Arbeitsbericht_NAB_12-23
Jackson, M., & Hudec, M. (2017). Salt tectonics. In *Salt tectonics: Principles and practice* (p. I). Cambridge University Press.
Jackson, M. P. A., & Talbot, C. J. (1986). External shapes, strain rates, and dynamics of salt structures. *Geological Society of America Bulletin, 97*, 305–323. https://doi.org/10.1130/0016-7606(1986)97%3c305:ESSRAD%3e2.0.CO;2
Karakonstantis, A., Pavlou, K., & Kapetanisis, V. (2019). Tomographic imaging of the Andravida blind strike-slip fault (Western Greece). *Journal of Geophysics, 63*, 1–14. https://geophysicsjournal.com/article/29
Katz, D. A. (2014). Kinetic sand. http://chymist.com/Kinetic%20Sand.pdf
Kempf, O., & Pfiffner, O. A. (2004). Early tertiary evolution of the North Alpine Foreland Basin of the Swiss Alps and adjoining areas. *Basin Research, 16*, 549–567. https://doi.org/10.1111/j.1365-2117.2004.00246.x
Kettermann, M., Urai, J. L., & Vrolijk, P. J. (2017). Evolution of structure and permeability of normal faults with clay smear: Insights from water-saturated sandbox models and numerical simulations. *Journal of Geophysical Research: Solid Earth, 122*, 1697–1725. https://doi.org/10.1002/2016JB013341
Klinkmüller, M., Schreurs, G., Rosenau, M., & Kemnitz, H. (2016). Properties of granular analogue model materials: A community wide survey. *Tectonophysics, 684*, 23–38. https://doi.org/10.1016/j.tecto.2016.01.017
Koopman, A., Speksnijder, A., & Horsfield, W. Y. (1987). Sandbox model studies of inversion tectonics. *Tectonophysics, 137*, 379–388. https://doi.org/10.1016/0040-1951(87)90329-5
Koyi, H. A. (2001). Modeling the influence of sinking anhydrite blocks on salt diapirs targeted for hazardous waste disposal. *Geology, 29*, 387–390. https://doi.org/10.1130/0091-7613(2001)029%3c0387:MTIOSA%3e2.0.CO;2
Laubach, S. E., Olsen, J. E., & Gross, M. R. (2009). Mechanical and fracture stratigraphy. *AAPG Bulletin, 93*, 1413–1426. https://doi.org/10.1306/07270909094
Madritsch, H. (2015). Outcrop-scale fracture systems in the Alpine foreland of central northern Switzerland: Kinematics and tectonic context. *Swiss Journal of Geosciences, 108*, 155–181. https://doi.org/10.1007/s00015-015-0203-2
Madritsch, H., Naef, H., Meier, B., Franzke, H. J., & Schreurs, G. (2018). Architecture and kinematics of the Constance-Frick Trough (Northern Switzerland): Implications for the formation of Post-Variscan Basins in the Foreland of the Alps and scenarios of their Neogene Reactivation. *Tectonics, 37*, 2197–2220. https://doi.org/10.1029/2017TC004945
Malz, A., Madritsch, H., Meier, B., & Kley, J. (2016). An unusual triangle zone in the external northern Alpine foreland (Switzerland): Structural inheritance, kinematics and implications for the development of the adjacent Jura fold-and-thrust belt. *Tectonophysics, 670*, 127–143. https://doi.org/10.1016/j.tecto.2015.12.025
Mandal, N., Dhar, R., Misra, S., & Chakraborty, C. (2007). Use of boudinaged rigid objects as a strain gauge: Insights from analogue and numerical models. *Journal of Structural Geology, 29*, 759–773. https://doi.org/10.1016/j.jsg.2007.02.007
Marchant, R., Ringgenberg, Y., Stampfli, G., Birkhäuser, P., Roth, P., & Meier, B. (2005). Paleotectonic evolution of the Zürcher Weinland (northern Switzerland), based on 2D and 3D seismic data. *Eclogae Geologicae Helvetiae, 98*, 345–362. https://doi.org/10.1007/s00015-005-1171-8
Mayolle, S., Soliva, R., Dominguez, S., Wibberley, C., & Caniven, Y. (2021). Nonlinear fault damage zone scaling revealed through analog modeling. *Geology, 49*, 968–972. https://doi.org/10.1130/G48760.1
Mazurek, M., Hurford, A., & Leu, W. (2006). Unravelling the multi-stage burial history of the Swiss Molasse Basin: Integration of apatite fission track, vitrinite reflectance and biomarker isomerisation analysis. *Basin Research, 18*, 27–50. https://doi.org/10.1111/j.1365-2117.2006.00286.x
Mengong, M. E., & Zulauf, G. (2007). The impact of strain rate on folding and boudinage under plane strain: Results from analogue modelling. *Geotectonic Research, 95*, 101–114. https://doi.org/10.1127/1864-5658/07/0095-0101
Mock, S., & Herwegh, M. (2017). Tectonics of the central Swiss Molasse Basin: Post-Miocene transition to incipient thick-skinned tectonics? *Tectonics, 36*, 1699–1723. https://doi.org/10.1002/2017TC004584
Mulugeta, G. (1988). Squeeze box in a centrifuge. *Tectonophysics, 148*, 323–335. https://doi.org/10.1016/0040-1951(88)90139-4
Nagra (2001). Sondierbohrung Benken—Untersuchungsbericht. Nagra Technical Report, NTB 00-01, Wettingen. https://nagra.ch/en/downloads/technischer-bericht-ntb-00-01-2/
Nagra (2019a). Preliminary horizon and structure mapping of the Nagra 3D seismics JO-15 (Jura Ost) in time domain. Nagra Working Report, NAB 18-34, Wettingen. https://nagra.ch/en/downloads/arbeitsbericht-nab-18-34-2/
Nagra (2019b). Preliminary horizon and structure mapping of the Nagra 3D seismics NL-16 (Nördlich Lägern) in time domain. Nagra Working Report, NAB 18-35, Wettingen. https://nagra.ch/en/downloads/arbeitsbericht-nab-18-35-2/
Nagra (2019c). Preliminary horizon and structure mapping of the Nagra 3D seismics ZNO-97/16 (Zürich Nordost) in time domain. Nagra Working Report, NAB 18–36, Wettingen. https://nagra.ch/en/downloads/arbeitsbericht-nab-18-36-2/
Nagra (2022): TBO Rheinau 1–1—Data Report. Nagra Working Report, NAB 22-03, Wettingen
Naylor, M. A., Laroque, J. M., & Gauthier, B. D. M. (1994). Understanding extensional tectonics: Insights from sandbox models. In F. Roure, N. Ellouz, V.

S. Shein, & I. Skvortsov (Eds.), *Geodynamic evolution of sedimentary basins* (pp. 69–83). International Symposium.
Panien, M., Schreurs, G., & Pfiffner, A. (2006). Mechanical behaviour of granular materials used in analogue modelling: Insights from grain characterisation, ring-shear tests and analogue experiments. *Journal of Structural Geology, 28*, 1710–1724. https://doi.org/10.1016/j.jsg.2006.05.004
Passchier, C. W., & Druguet, E. (2002). Numerical modelling of asymmetric boudinage. *Journal of Structural Geology, 24*, 1789–1803. https://doi.org/10.1016/S0191-8141(01)00163-8
Pfiffner, O.A. (1986). Evolution of the north Alpine foreland basin in the Central Alps. In P.A. Allen, & P. Homewood (Eds.). Foreland Basins (pp. 219–228). https://doi.org/10.1002/9781444303810.ch11
Ramberg, H. (1981). *Gravity, deformation and the earth's crust*. Academic Press.
Richard, P. (1989). Champs de failles au dessus d'un décrochement de socle: modélisations expérimentale. PhD Thesis. Université Rennes 1, France. https://hal.archives-ouvertes.fr/tel-00675425/
Richard, P. (1991). Experiments on fault reactivation in strike-slip mode. *Tectonophysics, 188*, 117–131. https://doi.org/10.1016/0040-1951(91)90318-M
Richard, P. D., Naylor, M. A., & Koopman, A. (1995). Experimental models of strike-slip tectonics. *Petroleum Geoscience, 1*, 71–80. https://doi.org/10.1144/petgeo.1.1.71
Ritter, M. C., Leever, K., Rosenau, M., & Oncken, O. (2016). Scaling the sandbox—Mechanical (dis) similarities of granular materials and brittle rock. *Journal of Geophysical Research: Solid Earth, 121*, 6863–6879. https://doi.org/10.1002/2016JB012915
Roche, O., Druitt, T. H., & Merle, O. (2000). Experimental study of caldera formation. *Journal of Geophysical Research, 105*, 395–416. https://doi.org/10.1029/1999JB900298
Roche, V., Childs, C., Madritsch, H., & Camanni, G. (2020). Layering and structural inheritance controls on fault zone structure in three dimensions: A case study from the northern Molasse Basin, Switzerland. *Journal of the Geological Society, 177*, 493–508. https://doi.org/10.1144/jgs2019-052
Rocher, M., Chevalier, F., Petit, C., & Guiraud, M. (2003). Tectonics of the Northern Bresse region (France) during the Alpine cycle. *Geodinamica Acta, 16*, 131–147. https://doi.org/10.1016/j.geoact.2003.05.001
Rowan, M. G., Urai, J. L., Fiduk, J. C., & Kukla, P. A. (2019). Deformation of intrasalt competent layers in different modes of salt tectonics. *Solid Earth, 10*, 987–1013. https://doi.org/10.5194/se-10-987-2019
Sanford, A. R. (1951). Analytical and experimental study of simple geological structures. *GSA Bulletin, 70*, 19–52. https://doi.org/10.1130/0016-7606(1959)70[19:AAESOS]2.0.CO;2
Schmatz, J., Vrolijk, P. J., & Urai, J. L. (2010). Clay smear in normal fault zones—The effect of multilayers and clay cementation in water-saturated model experiments. *Journal of Structural Geology, 32*, 1834–1849. https://doi.org/10.1016/j.jsg.2009.12.006
Schmid, T., Schreurs, G., Warsitzka, M., & Rosenau, M. (2020). Effect of sieving height on density and friction of brittle analogue material: Ring-shear test data of quarz sand used for analogue experiments in the tectonic modelling lab of the University of Bern. *GFZ Data Services*. https://doi.org/10.5880/fidgeo.2020.006
Schmid, T. C., Schreurs, G., & Adam, J. (2022). Characteristics of continental rifting in rotational systems: New findings from spatiotemporal high resolution quantified crustal scale analogue models. *Tectonophysics, 822*, 229174. https://doi.org/10.1016/j.tecto.2021.229174
Schori, M. (2021). The development of the Jura Fold-and-Thrust Belt: Pre-existing basement structures and the formation of ramps. PhD thesis. University of Fribourg, Switzerland. https://folia.unifr.ch/unifr/documents/313053
Schori, M., Zwaan, F., Schreurs, G., & Mosar, J. (2021). Pre-existing basement faults controlling deformation in the Jura Mountains Fold-and-Thrust Belt: Insights from analogue models. *Tectonophysics, 814*, 228980. https://doi.org/10.1016/j.tecto.2021.228980
Schreurs, G., Buiter, S. J. H., Boutelier, J., Burberry, C., Callot, J.-P., Cavozzi, C., Cerca, M., Chen, J.-H., Cristallini, E., Cruden, A. R., Cruz, L., Daniel, J.-M., Da Poian, G., Garcia, V. H., Gomes, C. J. S., Grall, C., Guillot, Y., Guzmán, C., Hidayah, T. N., … Yamada, Y. (2016). Benchmarking analogue models of brittle thrust wedges. *Journal of Structural Geology, 92*, 116–139. https://doi.org/10.1016/j.jsg.2016.03.005
Shipilin, V., Tanner, D. C., von Hartmann, H., & Moeck, I. (2020). Multiphase, decoupled faulting in the southern German Molasse Basin—Evidence from 3-D seismic data. *Solid Earth, 11*, 2097–2117. https://doi.org/10.5194/se-11-2097-2020
Sinclair, H. D., & Allen, P. A. (1992). Vertical versus horizontal motions in the Alpine orogenic wedge: Stratigraphic response in the foreland basin. *Basin Research, 4*, 215–232. https://doi.org/10.1111/j.1365-2117.1992.tb00046.x
Sommaruga, A., Eichenberger, U. & Marillier, F. (2012). Seismic Atlas of the Swiss Molasse Basin. Edited by the Swiss Geophysical Commission. *Matériaux pour la Géologie de la Suisse—Géophysique, 44*. https://www.geologieportal.ch/en/themes/fundamentals-of-geology/geophysics/seismic-atlas.html
Stewart, S. A. (2007). Salt tectonics in the North Sea Basin: A structural style template for seismic interpreters. *Geological Society, London, Special Publications, 272*, 361–396. https://doi.org/10.1144/GSL.SP.2007.272.01.19
Stewart, S. A., & Clark, J. A. (1999). Impact of salt on the structure of the Central North Sea hydrocarbon fairways. *Petroleum Geology Conference Series, 5*, 179–200. https://doi.org/10.1144/0050179
Strozyk, F., Van Gent, H., Urai, J. L., & Kukla, P. A. (2012). 3D seismic study of complex intra-salt deformation: An example from the Upper Permian Zechstein 3 stringer, western Dutch offshore. *Geological Society, London, Special Publication, 363*, 489–501. https://doi.org/10.1144/SP363.23
Talebian, M., Feilding, E. J., Funing, G. J., Ghorashi, M., Jackson, J., Nazari, H., Parsons, B., Priestley, K., Rosne, P. A., Walker, R., & Wright, T. J. (2004). The 2003 Bam (Iran) earthquake: Rupture of a blind strike-slip fault. *Geophysical Research Letters, 31*, L11611. https://doi.org/10.1029/2004GL020058
Toda, S., Kaneda, H., Okada, S., Ishimura, D., & Mildon, Z. K. (2016). Slip-partitioned surface ruptures for the Mw 7.0 16 April 2016 Kumamoto, Japan, earthquake. *Earth, Planets and Space, 68*, 188. https://doi.org/10.1186/s40623-016-0560-8
Viola, G., Odonne, F., & Mancktelow, N. S. (2004). Analogue modelling of reverse fault reactivation in strike–slip and transpressive regimes: Application to the Giudicarie fault system, Italian Eastern Alps. *Journal of Structural Geology, 36*, 401–418. https://doi.org/10.1016/j.jsg.2003.08.014
Von Hagke, C., Cederbom, C. E., Oncken, O., Stöckli, D. F., Rahn, M. K., & Schlunegger, F. (2012). Linking the northern Alps with their foreland: The latest exhumation history resolved by low-temperature thermochronology. *Tectonics, 31*, TC5010. https://doi.org/10.1029/2011TC003078
Von Hagke, C., Kettermann, M., Bitsch, N., Bücken, D., Weismüller, C., & Urai, J. L. (2019). The effect of obliquity of slip in normal faults on distribution of open fractures. *Frontiers in Earth Science, 7*, 18. https://doi.org/10.3389/feart.2019.00018
Vouillamoz, N., Mosar, J., & Deichmann, N. (2017). Multi-scale imaging of a slow active fault zone: Contribution for improved seismic hazard assessment in the Swiss Alpine foreland. *Swiss Journal of Geosciences, 110*, 547–563. https://doi.org/10.1007/s00015-017-0269-0
Vrolijk, P. J., Urai, J. L., & Kettermann, M. (2016). Clay smear: Review of mechanisms and applications. *Journal of Structural Geology, 86*, 95–152. https://doi.org/10.1016/j.jsg.2015.09.006
Warren, J.K. (2016). Solution mining and salt cavern usage. In: Evaporites: A geological compendium. Springer International Publishing Switzerland, pp 1303–1374. https://doi.org/10.1007/978-3-319-13512-0_13
Warsitzka, M., Závada, P., Jähne-Klingberg, F., & Krzywiec, P. (2021). Contribution of gravity gliding in salt-bearing rift basins—A new experimental setup for simulating salt tectonics under the influence of sub-salt extension and tilting. *Solid Earth, 12*, 1987–2020. https://doi.org/10.5194/se-12-1987-2021
Weijermars, R., & Schmeling, H. (1986). Scaling of Newtonian and non-Newtonian fluid dynamics without inertia for quantitative modelling of rock flow due to gravity (including the concept of rheological similarity). *Physics of the Earth and Planetary Interiors, 43*, 316–330. https://doi.org/10.1016/0031-9201(86)90021-X
Wesnousky, S. G. (2005). The San Andreas and Walker Lane fault systems, western North America: Transpression, transtension, cumulative slip and the structural evolution of a major transform plate boundary. *Journal of Structural Geology, 27*, 1505–1512. https://doi.org/10.1016/j.jsg.2005.01.015
Willett, S. D., & Schlunegger, F. (2010). The last phase of deposition in the Swiss Molasse Basin: From foredeep to negative-alpha basin. *Basin Research, 22*, 623–639. https://doi.org/10.1111/j.1365-2117.2009.00435.x

Withjack, M. O., & Callaway, S. (2000). Active normal faulting beneath a salt layer: An experimental study of deformation patterns in the cover sequence. *AAPG Bulletin, 8*, 627–651. https://doi.org/10.1306/C9EBCE73-1735-11D7-8645000102C1865D

Withjack, M. O., Olson, J., & Peterson, E. (1990). Experimental models of extensional forced folds. *AAPG Bulletin, 74*, 1038–1054. https://doi.org/10.1306/0C9B23FD-1710-11D7-8645000102C1865D

Yarushina, V. M., Makhnenko, R. Y., Podladchikov, Y. Y., Wang, L. H., & Räss, L. (2021). Viscous behavior of clay-rich rocks and its role in focused fluid flow. *Geochemistry, Geophysics, Geosystems, 22*, e2021GC009949. https://doi.org/10.1029/2021GC009949

Ziegler, P. A. (1992). European Cenozoic rift system. *Tectonophysics, 208*, 91–111. https://doi.org/10.1016/0040-1951(92)90338-7

Zulauf, J., Zulauf, G., Göttlich, J., & Peinl, M. (2014). Formation of chocolate-tablet boudins: Results from scaled analogue models. *Journal of Structural Geology, 68*, 97–111. https://doi.org/10.1016/j.jsg.2014.09.005

Zwaan, F., Chenin, P., Erratt, D., Manatschal, G., & Schreurs, G. (2021a). Complex rift patterns, a result of interacting crustal and mantle weaknesses, or multiphase rifting? Insights from analogue models. *Solid Earth, 12*, 1473–1495. https://doi.org/10.5194/se-12-1473-2021

Zwaan, F., Chenin, P., Erratt, D., Manatschal, G., & Schreurs, G. (2022a). Competition between 3D structural inheritance and kinematics during rifting: Insights from analogue models. *Basin Research, 34*, 824–854. https://doi.org/10.1111/bre.12642

Zwaan, F., Corti, G., Keir, D., & Sani, F. (2020). Analogue modelling of marginal flexure in Afar, East Africa: Implications for passive margin formation. *Tectonophysics, 796*, 228595. https://doi.org/10.1016/j.tecto.2020.228595

Zwaan, F., Rosenau, M., & Maestrelli, D. (2021b). How initial basin geometry in uences gravity-driven salt tectonics: Insights from laboratory experiments. *Marine and Petroleum Geology, 133*, 105195. https://doi.org/10.1016/j.marpetgeo.2021.105195

Zwaan, F., Schreurs, G., & Buiter, S. J. H. (2019). A systematic comparison of experimental set-ups for modelling extensional tectonics. *Solid Earth, 10*, 1063–1097. https://doi.org/10.5194/se-10-1063-2019

Zwaan, F., Schreurs, G., Gentzmann, R., Warsitzka, M., & Rosenau, M. (2018). Ring-shear test data of quartz sand from the Tectonic Modelling Lab of the University of Bern (CH). V. 1. GFZ data Services. https://doi.org/10.5880/fidgeo.2018.028

Zwaan, F., Schreurs, G., Madritsch, H., & Herwegh, M. (2022b). Analysis of analogue models testing the influence of rheologically weak layers and basal fault kinematics on deformation in the overburden. GFZ Data services. https://doi.org/10.5880/fidgeo.2022.032

Zwaan, F., Schreurs, G., Naliboff, J., & Buiter, S. J. H. (2016). Insights into the effects of oblique extension on continental rift interaction from 3D analogue and numerical models. *Tectonophysics, 693*, 239–260. https://doi.org/10.1016/j.tecto.2016.02.036

Zwaan, F., Schreurs, G., Ritter, M., Santimano, T., & Rosenau, M. (2018c). Rheology of PDMS-corundum sand mixtures from the Tectonic Modelling Lab of the University of Bern (CH). V. 1. GFZ data Services. https://doi.org/10.5880/fidgeo.2018.023

Zwaan, F., Schreurs, G., Rudolf, M., & Rosenau, M. (2022c). Ring-shear test data of feldspar sand from the Tectonic Modelling Laboratory at the University of Bern (Switzerland). GFZ Data services. https://doi.org/10.5880/fidgeo.2022.008

Publisher's Note